Stony Brook University

Laser Spectroscopy and Magneto-Optical Trapping of Rubidium Atoms

A Thesis Presented

by

David E. Sproles

to

The Graduate School

in Partial Fulfillment of the Requirements

for the Degree of

Master of Science

in

Physics

(Scientific Instrumentation)

Stony Brook University

December 2008

Stony Brook University

The Graduate School

David E. Sproles

We, the thesis committee for the above candidate for the Master of Science degree, hereby recommend acceptance of this thesis.

James E. Lukens
Professor, Department of Physics and Astronomy

Thomas K. Hemmick
Professor, Department of Physics and Astronomy

Michael M. Rijssenbeek
Professor, Department of Physics and Astronomy

Dominik A. Schneble
Thesis Advisor and Assistant Professor, Department of Physics and Astronomy

This thesis is accepted by the Graduate School.

Graduate School

Abstract of the Thesis

Laser Spectroscopy and Magneto-Optical Trapping of Rubidium Atoms

by

David E. Sproles

Master of Science

in

Physics

(Scientific Instrumentation)

Stony Brook University

2008

This thesis describes experiments on laser spectroscopy and magneto-optical trapping of ^{87}Rb atoms. We perform polarization spectroscopy with a novel high-power diode laser system. An ultrahigh vacuum apparatus in the 10^{-10} Torr regime has been built which allows trapping of ultracold clouds of rubidium atoms. These atoms can be moved in a mechanically translated magnetic trap from the trapping region into the lower pressure region of the system with minimal losses. We demonstrate magento-optical trapping of ultracold atoms, with atom numbers up to 10^{10} atoms and temperatures below 1mK, as observed by fluorescence imaging.

Contents

List of Figures

Preface

In the 1890s, Planck fought with equations derived from what he understood as 'first principles'[1]. In researching light emitted from thermal objects, if the energy of emitted radiation at a given frequency was an integer multiple of a fundamental value, everything worked. Planck is often quoted as saying the assumptions he made in late 1900 to arrive at his radiation law were "an act of desperation."[a] This integer multiple was his first reluctant step towards quantization.

Louis de Broglie took the next step. In his 1924 thesis, he suggested that matter could behave as a wave. In 1927 Davisson and Germer[3] published in Nature, describing their experiment where a narrow beam of electrons was directed at a crystal of nickel. One of two graphs in the two page paper shows the electron intensity varying in a clear diffraction pattern.

Also in 1924, Satyendra Nath Bose made significant advances; namely he came up with an entirely new method of deriving Planck's formula. He tried to publish on his own, but it required Einstein's support (which he gave emphatically[4]) to get it published. His paper is widely viewed as one of the seminal papers in quantum statistics. Therein the concept of degeneracy in counting photons[5] was introduced quite obliquely.

This fundamentally new concept led to Einstein writing a paper in 1924[6] on the quantum theory of monatomic ideal gases. Eventually this led to the idea of Bose-Einstein condensation, the culmination of all these works: coherent and overlapping matter wavefunctions. There were, however, serious technical difficulties in experimentally realizing these ideas. It would take decades to reach an entirely new way of cooling atoms to condensation.

When trying to bring atoms to Bose-Einstein condensation, there is a great deal more involved than simply making them cold. The volume of the 'container' holding them becomes quite relevant. Simply compressing a balloon changes nothing if there is no commensurate removal of heat. To quantify this

[a] It is said he made this comment in reference to depending on Boltzmann's theories at the last moment. He was not comfortable with their tenets[2].

concept, consider the de Broglie wavelength of an atom in motion,

$$\tilde{L} = \sqrt{\frac{\hbar^2}{k_B T}} \sqrt{\frac{2\pi}{M}} \tag{1}$$

This couples the temperature to a linear dimension. Combining this with the number density gives us the dimensionless phase-space density,

$$\rho \simeq n\tilde{L}^3 \tag{2}$$

The nitrogen in the air around you has a phase-space density of roughly $\sim 10^{-10}$. Liquid nitrogen (close to boiling, at atmospheric pressure) has a value of ~ 0.0008. To attain Bose-Einstein condensation, a phase-space density of ~ 2.6 is needed[7].[b]

In an experiment to create an ultracold cloud of atoms and eventually produce a BEC, many technologies[8] are required. Extremely low pressures, lasers for cooling[9, 10], lasers and magnetic fields for trapping (both optical[11] and magnetic) and construction of a conservative potential that can be adjusted (allowing evaporative cooling). The result is a nanokelvin cloud of atomic gas known as a Bose-Einstein Condensate.

In this thesis I will describe a specific implementation of laser cooling of ^{87}Rb atoms in a novel BEC apparatus. Laser cooling[9] is performed with a high-power diode laser system that is locked via a polarization spectroscopy[12] technique. Atoms are caught from background vapor and trapped in a six-beam vapor cell MOT.

This thesis is organized as follows: chapter one covers some basic theory of the interaction of a two-level atom with light. Chapter two discusses some of the concepts of laser spectroscopy and describes our spectroscopy technique and its implementation. Chapter three briefly describes some of the applicable theory of laser cooling and its application to the trapping of atoms in our setup. Chapter four gives an overview of the experimental apparatus which was set up in this thesis work, while chapter five briefly reviews imaging of cold atoms and the preliminary results obtained during that time.

[b] Interestingly, ^{4}He reaches this value very close to its superfluid transition temperature.

Acknowledgements

I would like to thank Prof. Schneble for his help in the lab and with this thesis. In the early days when we had just a laser, a few optics and a donated table, he would both teach and discuss the relevant design concepts and choices. Granted, I didn't have much to contribute to these 'discussions' beyond questions, but I learned a great deal. As the lab came together, he kept things organized and moving in a direction that was clear. Despite any frustrations, the lab was always a good place to work with an exciting atmosphere. It was a wonderful experience to see the system grow from a blank optical table to a working, well tuned MOT. Seeing the BEC results and more recently atom diffraction across a lattice is very exciting!

I'd like to thank all of the students in the group for their many contributions. Especially Rebekah Schiller for her bright attitude and help all along, Daniel Pertot for his good nature and his patience in our collaboration on the TOP coils and last but certainly not least Hartmut Ruf for his help with collecting and analyzing data and in general for being an entertaining and very helpful labmate. While I have not worked closely with all the students in the lab, nearly everyone has made a contribution to the group which in some way affected this thesis: thank you all for your help.

I'd like to thank my parents for their interest in my work and for supporting me through my trials in all of college, both rounds. I definitely need to thank my late grandmother, Ruby Farmer, for her contributions to my education and other aspects of my life, culinary and spiritual. Lastly I'd like to thank my friends for tolerating me as I worked and for encouraging me; in particular (and no discernable order) Mike A., Steve F., Evan B., Katie F., Livy K., Daniel S., Jay S., the Parsons (congratulations!), the Lichtenbergs, Frank McW., Alice L., all of WFDL1 (may it rest in pieces) and (though only briefly... twice...) SFWE, and all of LGBTA and its orbiting grads. I don't know if I could have made it this long without you.[c]

[c]Triple entendre intentional.

Chapter 1

Atoms in Light Fields

In this chapter I will discuss a classical model of the interaction of light with atoms. The effect of a light field on transitions will be explored and equations will be set up for the development of spectroscopy and laser cooling in later chapters.

1.1 Lorentz Model

A classical view of the interaction of atoms with light will suffice for many of the effects relevant to laser cooling. A straightforward model developed by Lorentz[13] begins with the following view of the atom: consider the electron as bound to the nucleus by a linear restoring force characterized by a 'spring constant' k. The applied electric field (from a light wave traveling in the z-direction) is given as $\vec{E}(z,t)$. A linear restoring force and the applied driving

force of this electric field mean we have a driven harmonic oscillator[a]:

$$m_e \times {\partial_t}^2 \vec{x} = e\vec{E}(z,t) - k\vec{x}$$
$$({\partial_t}^2 + {\omega_0}^2)\vec{x} = \frac{e}{m_e}\vec{E}(z,t),$$

with $\omega_0 \equiv \sqrt{\frac{k}{m_e}}$ as the resonance frequency. In this model the atom's interactions with light fields are characterized by ω_0. Including a damping term β in the oscillator equation will allow many more details to be revealed. The source for this damping term will be covered later. Take the applied light field as $\vec{E} = \hat{x}E_0 e^{-i(\omega t - kz)}$,

$${\partial_t}^2 \vec{x} + 2\beta\partial_t \vec{x} + {\omega_0}^2 \vec{x} = \hat{x}\frac{e}{m}E_0 e^{-i(\omega t - kz)}$$

By assuming the solution has the form $\vec{x} = \vec{a}e^{-i(\omega t - kz)}$ the electron's oscillation amplitude is given by

$$\vec{a} = \hat{x}\frac{(e/m)E_0}{({\omega_0}^2 - \omega^2) - 2i\beta\omega} \tag{1.1}$$

The polarization of an atom is defined as $\vec{p} = e\vec{x}$. The polarization density of a bulk gas (with number density N) is $\vec{P} = Ne\vec{x}$; define $\alpha(\omega)$ such that $\vec{P} = N\vec{E}\alpha(\omega)$. Let $\tilde{\omega}^2 \equiv ({\omega_0}^2 - \omega^2)$:

$$\alpha(\omega) = \frac{e^2/m}{\tilde{\omega}^2 - 2i\beta\omega} \tag{1.2}$$

[a]The nucleus must be assumed stationary, which is reasonable given the mass ratio.

By using Maxwell's equations and a vector identity, we have $\vec{\nabla}^2\vec{E} - \frac{1}{c}{\partial_t}^2\vec{E} = \frac{1}{\epsilon_0 c}{\partial_t}^2\vec{P}$. The assumed form for the electric field reduces this to

$$\begin{aligned} -k^2 + \frac{\omega^2}{c^2} &= N\frac{-\omega^2}{\epsilon_0 c}\alpha(\omega) \\ \left(\frac{kc}{\omega}\right)^2 &= 1 + N\frac{\alpha}{\epsilon_0} \\ n^2(\omega) &= 1 + N\frac{\alpha}{\epsilon_0} \end{aligned} \tag{1.3}$$

Here $n = \frac{kc}{\omega}$ is the index of refraction of the gas; for a dilute atomic gas, α is small and n is approximately one. Expanding to first order and approximating $\tilde{\omega}^2 \approx 2\omega(\omega_0 - \omega)$ leads to

$$n = \underbrace{1 + \frac{1}{2}\frac{Ne^2}{\epsilon_0 m}\frac{\tilde{\omega}}{2\omega(\omega_0 - \omega) + 4\beta\omega^2}}_{\text{dispersive}=n'} + i\underbrace{\frac{1}{2}\frac{Ne^2}{\epsilon_0 m}\frac{2\beta}{2(\omega_0 - \omega) + 4\beta^2\omega}}_{\text{absorptive}=\alpha} \tag{1.4}$$

$$n = n' + i\alpha$$

The two components of this complex index of refraction are called the Kramers-Kronig dispersion relations. The absorptive component can be rewritten in terms of frequency $\nu \equiv \omega/2\pi$ and $\delta\nu_0 \equiv \beta/2\pi$. This introduces the Lorentzian lineshape function $L(\nu)$;

$$\begin{aligned} L(\nu) &= \frac{\delta\nu_0/\pi}{(\nu - \nu_0)^2 + {\delta\nu_0}^2} \\ a(\nu) &= \frac{Ne^2}{4\epsilon_0 mc}L(\nu) \end{aligned} \tag{1.5}$$

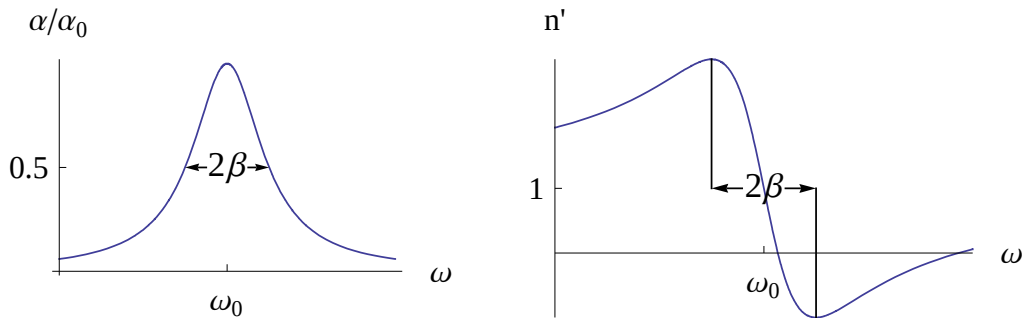

Figure 1.1: Graphs of the absorption and dispersion curves from the Kramers-Kronig dispersion relations. Here 2β denotes the linewidth of the resonance[14], which is ultimately limited by the natural linewidth of the transition (see Sec. 2.1.1). This width can and will be affected by many other factors, discussed in Chapter 2.

The plots in Fig. 1.1 are central to the upcoming sections; the lineshape of n is an estimate of sharpness of the transition feature that can be obtained. Several effects discussed below tend to blur this response curve and obscure spectroscopic information.

The Lorentz model comes very close to predicting good values for optical transitions. The theory is patched by considering that the 'oscillator' has a proscribed 'strength', determined experimentally for each transition.

$$e^2 \rightarrow fe^2 : a_i(\nu) = \frac{Nf_ie^2}{4\epsilon_0 mc} L(\nu) \tag{1.6}$$

This patch to the theory was developed from experimental observations, but has an explanation originating in quantum mechanics. The use of oscillator strengths provides sufficient freedom to bring the Lorentz model into good agreement with experimental results.

1.2 Two-Level Atoms

The Lorentz model approximates the behavior of a gas (in the limit of low excitation). A more accurate description for stronger fields requires a semiclassical approach, which also captures the internal level structure of the atoms.

Let's begin with the Schrödinger equation for a two-level system, with energies given as E_1 and E_2 and interaction matrix elements with the electromagnetic field given by $\tilde{U}_{ij} =< \Psi_i|U|\Psi_j >= -\frac{1}{2}e\hat{\epsilon}(E_0e^{-i\omega t} + c.c.) < \vec{r} >_{ij}$. Parity arguments leave the diagonal elements as zero, leaving us with

$$i\hbar \begin{pmatrix} \dot{a}_1 \\ \dot{a}_2 \end{pmatrix} = \begin{pmatrix} E_1 & \tilde{U}_{12} \\ \tilde{U}_{21} & E_2 \end{pmatrix} \begin{pmatrix} a_1 \\ a_2 \end{pmatrix}$$

From here we set our ground state energy $E_1 = 0$, define the transition energy by its frequency $\omega_{21} \equiv \frac{E_2 - E_1}{\hbar}$ and define the applied light field strength according to the Rabi frequency, given as

$$\chi_{ij} \equiv e\left(\langle\vec{r}\rangle_{ij} \cdot \hat{\epsilon}\right)\frac{E_0}{\hbar} \tag{1.7}$$

Near resonance $\omega \simeq \omega_{21}$ is a good approximation. Now we apply the rotating wave *transformation*: $a_1(t) = c_1(t)$ and $a_2(t) = c_2(t)e^{-i\omega t}$, and obtain

$$i \begin{pmatrix} \dot{c}_1 \\ \dot{c}_2 \end{pmatrix} = \begin{pmatrix} 0 & -1/2\left(\chi_{21}^* + \chi_{12}e^{-i2\omega t}\right) \\ -1/2\left(\chi_{21} + \chi_{12}^* e^{i2\omega t}\right) & \omega_{21} - \omega \end{pmatrix} \begin{pmatrix} c_1 \\ c_2 \end{pmatrix} \tag{1.8}$$

The rotating wave *approximation* asserts that $e^{-i2\omega t}$ will be much faster than atomic evolution, leaving those quantities averaged out. Define the detuning

Δ as $\omega_{21} - \omega$ and letting $\chi = \chi_{21}$;

$$i\dot{c_1} = -1/2\chi^* c_2$$
$$i\dot{c_2} = \Delta c_2 - 1/2\chi c_1$$

With the assumption that the Rabi frequency (and thus the electric field strength) is real, $\chi \in \mathbb{R}$, and the definition $\Omega = \sqrt{\chi^2 + \Delta^2}$ we can solve these equations as

$$c_1(t) = \left(\cos\left(\frac{\Omega t}{2}\right) + i\frac{\Delta}{\Omega}\sin\left(\frac{\Omega t}{2}\right)\right) e^{-i\Delta t/2}$$
$$c_2(t) = \left(i\frac{\chi}{\Omega}\sin\left(\frac{\Omega t}{2}\right)\right) e^{-i\Delta t/2}$$

Here Ω is the *generalized* Rabi frequency; the frequency of oscillations between the two levels.

From this point we can build the density matrix from the equations for the $c_i(t)$ equations. This matrix[b] will allow us to include the details of population transfer explicitly: collisions and spontaneous emission specifically.

$$\rho \equiv \begin{pmatrix} c_1 c_1^* & c_1 c_2^* \\ c_2 c_1^* & c_2 c_2^* \end{pmatrix} = \begin{pmatrix} \rho_{ee} & \rho_{eg} \\ \rho_{ge} & \rho_{gg} \end{pmatrix} \tag{1.9}$$

Here the index "e" ("o") denotes the excited (ground) states of the system.

These can be solved to give more general population density equations. In full detail, one includes loss rates from each level (out of the 2-level system) due

[b] In this matrix there are only three independent quantities; Feynman[15] noticed this and suggested a very intuitive description of the two level system.

to atomic collisions (Γ) and spontaneous emission rates A_{21}. For our timescales and pressures, loss rates out of the system due to collisions are exceedingly low.

$$\left.\begin{aligned} \dot{\rho_{gg}} &= \underbrace{-\cancel{\Gamma_1\rho_{11}}}_{coll.} \underbrace{+A_{21}\rho_{ee}}_{spont.emmis.} - i/2(\chi\rho_{ge} - \chi^*\rho_{eg}) \\ \dot{\rho_{ee}} &= \underbrace{-\cancel{\Gamma_2\rho_{22}}}_{coll.} \underbrace{-A_{21}\rho_{ee}}_{spont.emmis.} + i/2(\chi\rho_{ge} - \chi^*\rho_{eg}) \end{aligned}\right\} \tag{1.10}$$

Through several approximations and via multiplying by atomic density, we obtain the population rate equations

$$\left.\begin{aligned} \dot{N_e} &= A_{21}N_g + \sigma\Phi(N_g - N_e) \\ \dot{N_g} &= -A_{21}N_g - \sigma\Phi(N_g - N_e) \end{aligned}\right\} \tag{1.11}$$

where σ is the atomic absorption cross section and Φ is the photon flux.

These are the population rate equations for a two level system. Solving yields

$$N_g(t) = \left[N_g(0) - \frac{N\sigma\Phi}{A_{21} + 2\sigma\Phi}\right] e^{-(A_{21}+2\sigma\Phi)t} + \frac{N\sigma\Phi}{A_{21} + 2\sigma\Phi} \tag{1.12}$$

We can now use these equations to establish some of the principles of spectroscopy and laser cooling.

Chapter 2

Spectroscopy of Rubidium

In this chapter, laser stabilization and control will be discussed. Level structure involved in spectroscopy and relevant cooling transitions will be discussed, as will laser design allowing tight control of emitted wavelength.

2.1 Spectral Broadening Mechanisms

The stability of the lasers used will determine the final stability of the atomic trap as well as the precision, accuracy and reliability of imaging. The lasers produce light at hundreds of THz, must be tunable on the scale of GHz yet also must be stable on the scale of the linewidth (several MHz) of the transitions that will be used. To meet these requirements, high performance frequency metrology is needed alongside electronic feedback in order to lock the lasers to the correct transitions. The required well-characterized error signal is obtained via spectroscopy.

Several effects will broaden the frequency response of atoms to light fields.

While these broadening effects do not play a role in dilute, ultracold atomic clouds, they exist in relatively high pressure spectroscopy vapor cells, and must be thwarted to make frequency control possible. Some of these effects are negligible and easily counteracted while some require clever techniques to manage.

2.1.1 Spontaneous Decay

There are several ways to derive the natural linewidth of transitions; one acceptable, if pedestrian, way is to consider the uncertainty principle[14]. Excited states (energy E_e) have decay rates and mean lifetimes (τ_e). Such a lifetime fits naturally into the Heisenberg relation: $\Delta E_e \simeq \frac{\hbar}{\tau_e}$. Given that this excited state decays into the ground state, E_g, the frequency of emitted light will be $\omega_{decay} = (E_e - E_g)/\hbar$ with an uncertainty based on that of the excited state:

$$\Delta\omega = \gamma \simeq \Delta E_e/\hbar. \tag{2.1}$$

This gives us the natural linewidth of the transition of our two-level system. This is a fundamental limit. For the relevant transition to cooling Rubidium[a], the natural linewidth is $2\pi * 6.0666(18)$MHz[16].

2.1.2 Collisional/Pressure Broadening

In the classical oscillator model in Ch. 1, a 'friction' term (β) was introduced but little explanation provided. It eventually determined the width of the

[a] $5^2S_{1/2} \rightarrow 5^2P_{3/2}$

resonance. As stated above, it has a minimum value, but many effects can contribute to it. This term in the equation of motion can be justified by electron 'dephasing'; within the framework of the model, it is reasonable to understand collisions with other atoms as affecting the electron's displacement and thus resetting the oscillator's phase. Consider a collection of atoms all set in motion together. Each collision will change the phase of oscillation which will, on average across the collection, cause the electron oscillations to be damped. This damping (i.e. 'friction') will broaden the frequency response, leading to decreased accuracy in determining the specific wavelengths associated with transitions. In a spectroscopy cell, this is clearly unacceptable as our lasers must be stabilized to the order of the natural linewidth.

The easiest solution to reduce collisional broadening is to isolate the sample of atomic gas in a low-pressure environment, as with our reference vapor cell. Too low a pressure obviously presents its own problems with regards to maintaining gas purity at that pressure; regardless of this difficulty, simply decreasing the pressure in the cell is insufficient. Collisions with walls are no different than collisions with other gas atoms: decreasing the pressure will only reduce the frequency of collisions up to a point, beyond which the atoms will be bouncing off the walls. The solution lies in noble gases, which are symmetric and spinless. Collisions with them are significantly less likely to dephase the electron's oscillations.[17, 18] This constrains the background gas pressure to an ideal value, maximally reducing wall collisions without serious broadening from noble-gas collisions. This keeps the pressure in the reference at a level requiring nothing more than the glass walls to maintain it at the requisite gas purity.

2.1.3 Power Broadening

Let us pick up 1.9 where we left off. The earlier solutions were only for ρ_{gg} and ρ_{ee}. If instead solved for ρ_{ge} and ρ_{eg} one again pulls out β. In this context, we are only considering light effects on isolated atom(s), thus β is the relaxation time and is dominated by $1/\tau$, the decay time of the excited state.

Continuing with Eq. 1.10, dropping the first term in the high-power (Φ large) and long time limit yields:

$$\rho_{ee} = \frac{N_2(t \to \infty)}{N} = \frac{\sigma\Phi/A_{21}}{1 + 2\sigma\Phi/A_{21}} \tag{2.2}$$

$$= \frac{\chi^2\beta/2A_{21}}{\Delta^2 + (\beta^2 + \chi^2\beta/A_{21})}, \tag{2.3}$$

with $\chi \propto E_0$, where E_0 is the electric field strength. Here we have a Lorentzian shape dependent on the Rabi frequency. More power results in higher Rabi frequency; this will broaden the lineshape.

Qualitatively, power broadening is a result of transition saturation. The light field intensity is such that many atoms are in the excited state, leaving fewer atoms available for absorption near the transition. Away from the transition less saturation occurs, leaving more atoms available for absorption.

The easiest solution to this problem is to use weak pump and probe beams. Detectors can be fitted with inexpensive line filters that will restrict sensitivity to laser light only, avoiding ambient contributions.

2.1.4 Doppler Broadening

The Doppler effect refers to the frequency shift of an observed electromagnetic wave due to atomic motion along the wave's direction of propagation. This effect is central to spectroscopy as well as cooling processes. Given light propagating in the $\hat{k}$ direction and an atom's velocity (nonrelativistic, of course) as $\vec{v}$

$$\nu_{\text{absorbed}} = \nu_{\text{emitted}}(1 - \frac{\vec{v} \cdot \hat{k}}{c}) \tag{2.4}$$

The usual terminology is to refer to the absorbed light as blue- or red-shifted in the reference frame of the atom; blue-shifted light increases the frequency and energy, red-shifted vice versa. Let us briefly look at the velocity distributions present in a gas of atoms.

Velocity Distributions

There are two ways to view the distribution of atomic velocities; the velocity of atoms along one specific direction (orthogonal velocities count as zero along the direction of interest; Fig. 2.1b) vs. the velocity of atoms in any given direction (spherical, integrating all velocities as positive; Fig. 2.1a). Let $\tilde{v} \equiv \sqrt{k_B T/M}$. This is the characteristic thermal velocity of the atoms, based on temperature. The Maxwell-Boltzmann distribution is given by

$$S_{3D}(v) = \sqrt{\frac{2}{\pi}} \frac{v^2}{\tilde{v}^2} exp\left(-\frac{v^2}{2\tilde{v}^2}\right) \tag{2.5}$$

$$S_{1D}(v) = \frac{1}{\sqrt{2\pi}\tilde{v}} exp\left(-\frac{v_x^2}{2\tilde{v}^2}\right) \tag{2.6}$$

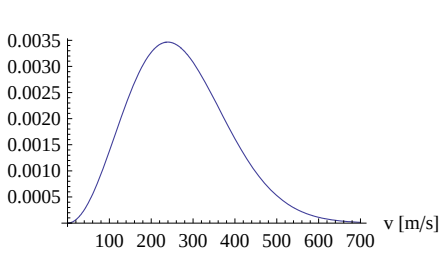

(a) $S_{3D}(v)$ MB distribution in 3D.

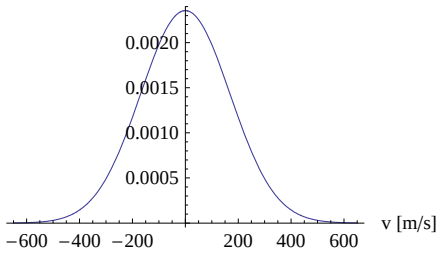

(b) $S_{1D}(v)$ MB distribution in 1D.

Figure 2.1: The Maxwell-Boltzmann distributions for ^{87}Rb atoms at room temperature.

The idea of laterally moving atoms is significant to Doppler-free spectroscopy; primarily of interest to this section is the 3D distribution of velocities.

Lineshape Function

The stochastic thermal motion of atoms leads to inhomogeneous spectral broadening via the Doppler shift; some atoms will absorb red-shifted light and some absorb blue-shifted light. Putting the one-dimensional Maxwell-Boltzmann distribution together with the Doppler shift yields the lineshape function for Doppler broadening. Taking T as the gas temperature in Kelvin, M as the molecular weight of the gas and λ_0 as the wavelength in Å, one obtains[13]

$$S(v) = \frac{1}{\delta v_D}\left(\frac{4\ln 2}{\pi}\right)^{1/2} e^{-4\ln 2(v-v_0)^2/\delta v_D^2}\frac{1}{\text{MHz}} \tag{2.7}$$

$$\delta v_D = 2.15\times 10^6\left[\frac{1}{\lambda_0}\left(\frac{T}{M}\right)^{1/2}\right]\text{MHz} \tag{2.8}$$

Substituting in the values for Rubidium atoms at room temperature:

$$\delta v_D = 2.15 \times 10^6 \left[\frac{1}{7806\text{Å}} \left(\frac{298K}{85.5g} \right)^{1/2} \right]$$

$$\delta v_D \approx 514\text{MHz}$$

This calculation yields the width for an isolated transition of room-temperature atoms as measured by one directed beam.

The linewidth of the transition to which we must stabilize is roughly 6 MHz. While the Doppler broadening of a transition by hundreds of MHz seems severe, there are techniques to overcome this apparently large difficulty.

2.2 Spectroscopy; Doppler-Free Techniques

All methods used to overcome Doppler broadening are built on the idea of counter-propagating beams. Light from a laser is split into a probe and pump beam; these beams are sent through the gas sample in opposite directions. Fig. 2.2 illustrates this.

In three dimensions large numbers of atoms can move orthogonally to the pump-probe axis. These atoms can interact with both beams at the rest-frame frequency. For atoms moving along the pump-probe axis there will be Doppler shifts in opposite directions for each beam. The result is that, for off-resonance frequencies, each beam will interact with different classes of atoms. From this general Doppler-free setup there are two easy ways that spectroscopy data can be obtained.

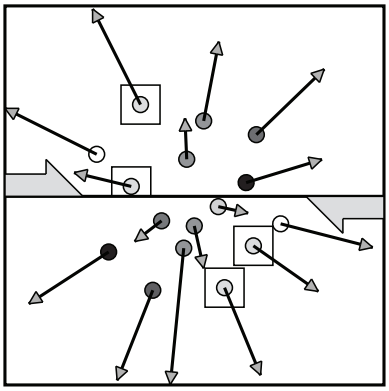

(a) Atoms with thermal velocity, only (x,y) shown.

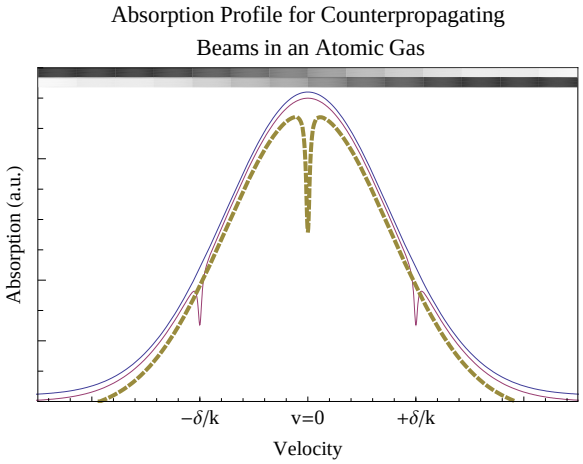

(b) Plot of absorption vs. velocity.

Figure 2.2: Doppler shift and counter propagating beams (of wavevector $\pm k\hat{x}$). (a) A collection of thermal atoms with random x-y velocity (z not shown). The atoms are shaded according to 'observed' frequency. Boxes are drawn around different classes of atoms resonant with their respective beam. The top has a right-propagating beam, the lower is left-propagating. (b) A graph of absorption dependent on velocity for a laser detuned from ν_{res} by δ. Atoms traveling *along* a beam's propagation direction will absorb according to a lab-frame-velocity of $v = (\nu_{res} - \delta)/k$, while atoms traveling *against* will absorb at a lab-frame-velocity of $(\nu_{res} + \delta)/k$. When the Bennet holes overlap (this condition shown by the dashed curve), both directional beams will then interact with the same velocity-group of atoms. This drop in absorption (for each beam) is called a Lamb dip.

2.2.1 Saturation Spectroscopy

Saturation spectroscopy works by saturating the transitions via the pump beam. The pump beam will reduce the population in the lower level of that transition. The probe beam will then experience reduced absorption (thus more light will pass through) near that frequency. Fig. 2.2 shows a sketched absorption spectrum in velocity space; the small dips in grey refer to the effect of each beam and are called Bennet holes[14]. When the laser is on resonance these 'holes' in the spectrum will overlap; that drop in absorption is called a Lamp dip[13].

By scanning the laser through the frequencies around this transition, we can obtain the transition spectrum. This spectroscopy signal is now free of Doppler broadening.

One of the technical difficulties with saturation spectroscopy is that the center of the transition is located at a point where the signal has no slope. Scanning the laser continuously to see the resonance goes directly against the idea of a stabilized laser. To generate a signal for feedback, a dispersive shape is required. Phase-sensitive detection (e.g. a lock-in amplifier) is needed to generate a dispersively shaped signal. The complexity of the setup can be bypassed as discussed in the next section.

2.2.2 Polarization Spectroscopy

From one perspective polarization spectroscopy works in much the same way as saturation spectroscopy; rather than recovering signal from the absorptive component of Eq. 1.4, the dispersive index of refraction serves as the source.

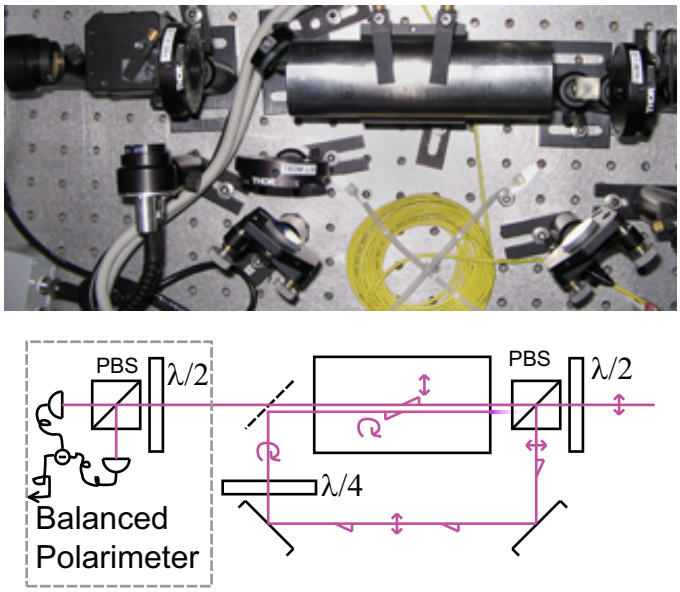

Figure 2.3: Balanced polarimeter. The input beam comes from the right and is sent through a proportional splitter, allowing the ratio of pump/probe amplitude to be adjustable. A 50/50 non-polarizing beamsplitter is used to redirect the pump beam backwards through the vapor cell and allow the partially attenuated probe beam through to the balanced polarimeter. The half-waveplate allows the polarimeter to be balanced according to maximum dispersive signal strength.

From another point of view, polarization spectroscopy is entirely different in that it makes use of the multi-level structure of atoms. This method avoids intensive signal processing: light-induced birefringence generates a dispersive signal that can be directly fed into the feedback loop.

The setup for polarization spectroscopy is shown in Fig. 2.3. A more intense σ^+ polarized pump beam pushes each lower-level electron into a 'higher'[b] magnetic sublevel. This is called optical pumping[14], leading to nearly all the population undergoing Rabi oscillations between the highest possible magnetic sublevels of the ground state and the possible sublevels of the excited states

[b]With respect to the quantization axis defined by the pump beam.

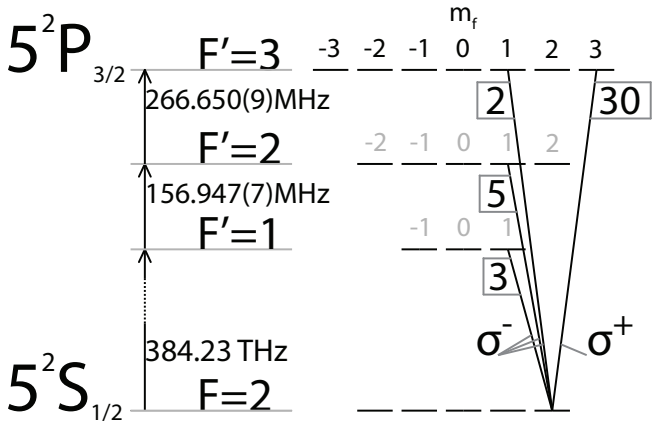

Figure 2.4: Schematic of available transitions. Clebsch-Gordon coefficients indicated in boxes for each transition.[9, 16]

(Fig. 2.4.)

Consider the appropriate sublevels of the excited states. Each transition to either higher or lower m_F will have a strength (stronger causing more absorption), determined by calculating the Clebsch-Gordon coefficients. See Fig. 2.4 for the strengths[9]. If, for one F, the $m_F + 1$ and the $m_F - 1$ have different strengths, then σ^+ and σ^- beams will experience different indices of refraction. The probe beam is linearly polarized. It can be decomposed into left- and right-circularly polarized components. The difference in the transition coefficients determines the difference in optical 'thickness' for one component versus the other. Thus, a 'tilt' of the linear probe beam's polarization develops, which we will call $\Delta\phi$. Given a length of vapor L, the linear probe beam will have its polarization rotated by

$$\Delta\phi = (k^+ - k^-)L = (\omega L/c)(n^+ - n^-) \tag{2.9}$$

The indices of refraction are given by the n' component of Eq. 1.4. The difference between transition strengths for the σ^+ and σ^- determines both the sign and the magnitude of $\Delta\phi$.

The rotation of the pump's polarization can be detected by blocking one linear component and measuring the transmission of the other. If a balanced polarimeter is used instead, the signal magnitude is increased and some background effects are diminished or removed. Some of the background is due to the birefringence of vapor cell's windows. This only results in a small linear offset[19] which is easily compensated via the optics in the balanced polarimeter. This polarimeter is set up with a half-waveplate and a polarizing beamsplitter. The two photodiode signals are then subtracted. Torii and Kuga[12] give the transmission[c] of this balanced polarimeter as

$$\Delta I_t = I_t(45^o) - I_t(-45^o) \tag{2.10}$$

$$= 2I_0 e^{-\alpha L}\Delta\phi \tag{2.11}$$

Here α is the absorptive component from Eq.1.4. The output polarization of the linearly-polarized probe beam is rotated according to distance from the center of the transition. The signal for the polarimeter is dispersive in shape and resembles the index of refraction graph in Fig. 1.1.

In practice, setting up this spectroscopy is straightforward. The angle of the half-waveplate in the balanced polarimeter is set experimentally according to minimized background across the whole transition in question. If care is

[c]Please note that we have glossed over the effects of gas density in the vapor cell; this will obviously scale the effect, but does not change functional form.

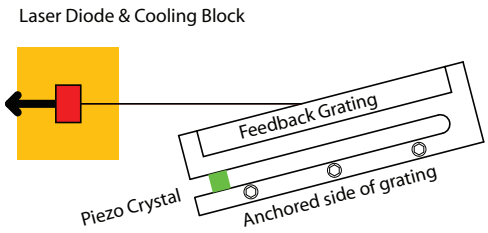

Figure 2.5: Setup for rear-coupled ECDL. Note the lever arm used by the piezo to modulate the cavity length.

used, the diode signals can simply be wired against each other in a circuit. For greater certainty, a simple op-amp circuit can be used to subtract the signals.

The most attractive feature of this design is the lack of equipment required. No phase sensitive detection is needed to extract a dispersive signal; the output can be fed directly into a laser's control circuit, closing the feedback loop.

2.3 Laser Design

Each of the lasers in our lab is an extended cavity diode laser (ECDL) set up roughly as in Ref. [20]. Relevant to the control of the laser system is the piezo-mounted grating. The rapid response time and ease of incorporation into control loops of this setup is ideal.

For the Sacher laser, one relevant modification to this ECDL setup is that the tuning grating is set up on the rear facet of the diode. See Fig. 2.5. The majority of the power is output via the opposing facet. The advantage of the rear-face coupled design is the lack of angular modulation of the output beam as various frequency settings are adjusted to find a good operating point. The Toptica laser is not rear-coupled.

This design modulates the frequency not by the variation of the angle of

the grating, for that effect is trivial on the relevant scale. Instead, the rear facet of the diode and the grating form a cavity, external to the laser. As the cavity length varies, so does the frequency. The cavity length must contain an integer number of half-wavelengths; for small perturbations around a given optimal longitudinal mode, the frequency will shift, rather than the number of wavelengths in the cavity. The external cavity length (L_{ec}) contains many (n_{ec}) wavelengths[d]: $L_{ec} = n_{ec}\lambda$. Thus any change in external cavity length, ΔL_{ec} results in a fractional wavelength change, $\Delta\lambda = \frac{\Delta L_{ec}}{n_{ec}}$. A modest piezo that would fit into the laser system shown in Fig. 2.5 can generate maximum deflection to the scale of hundreds of nanometers, with resolution approaching (many) tenths of a nanometer: about a factor of 1000, usually more. Combined, these effects produce the requisite fractional adjustment of better than 1:1,000,000 in terms of smallest input shift to frequency modulation.

2.4 Feedback and Results

For isolated transitions, the observed spectrum will conform to the conclusions above. If there are several closely spaced transitions, however, the observed spectrum will require further analysis. For example, consider transitions from ground state 'A' to levels '1' or '2'. Given a source laser slightly detuned such that the laser frequency, ν_l, lies between the transition frequencies of A→1 (ν_1) and A→2 (ν_2), an atom could be moving at a velocity causing it to absorb $\nu_1 + \nu_{Dopp}$ and $\nu_2 - \nu_{Dopp}$, both of which can equal ν_l. The detector will observe a transition where there isn't one. This type of interaction is called a crossover

[d] A 5mm external cavity would contain about 6,500 wavelengths.

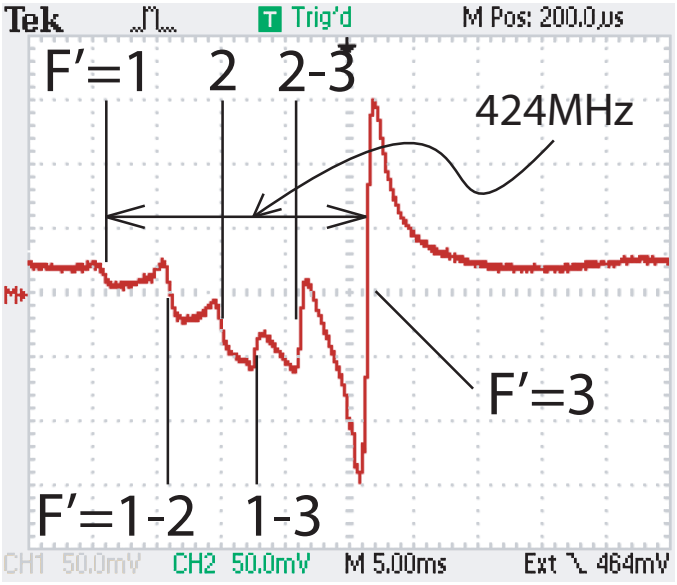

Figure 2.6: Oscilloscope trace of a balanced polarimeter signal of the $5S_{1/2}F = 2 \rightarrow 5P_{3/2}F'$ transition in ^{87}Rb. Crossover resonances are labeled. Vertical units are photodiode voltage (thus arbitrary).

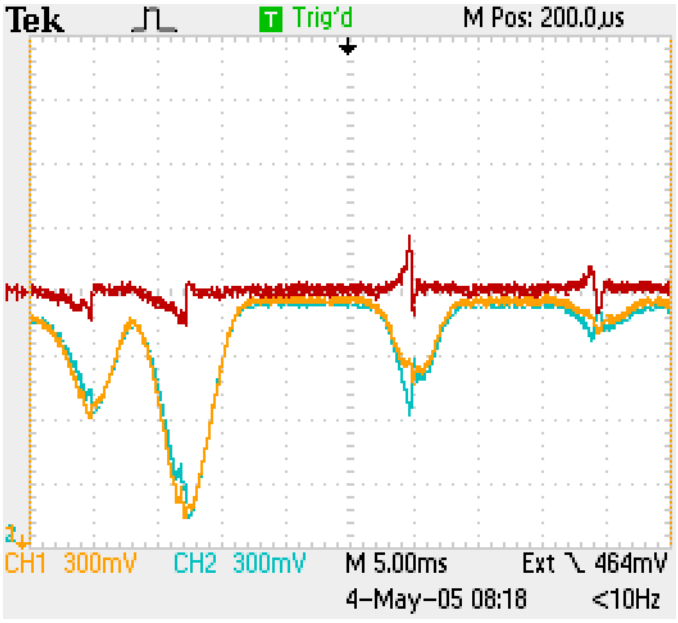

Figure 2.7: A full trace of the transitions of ^{87}Rb that will be used for trapping. The width of this scope trace is ≈ 7.2 Ghz.[16] The lower traces are the separate diodes of the balanced polarimeter and clearly show Doppler broadening.

resonance. They were observed in our spectra and are labeled in Fig. 2.6.

Coupling the spectroscopy signal to the laser control electronics, the feedback loop is closed and the laser is locked to the correct transition. The feedback loop parameters (gain, damping, offset) are set experimentally to obtain the best lock. See Fig. 2.7 for a full scan of all the levels discussed in Chapter One. Figure 2.6 shows a closeup scan of the cycling transition lockpoint.

Chapter 3

Magneto-Optical Cooling and Trapping

Light carries momentum; light interacting with atoms allows us to engineer forces such that cooling and confinement of atoms is possible. To accomplish trapping[a], magnetic fields will be combined with light from the carefully stabilized lasers of the previous chapter.

In this chapter we will first discuss cooling and temperature of atoms, moving on to a simplistic model of atomic trapping. Lastly the loading of such a trap is covered.

3.1 The Scattering Force

The force of laser light on atoms is a consequence of the asymmetry between directed absorption from a laser field and random spontaneous emission. On

[a] All optical traps are possible, but will not be covered in this document.

average, spontaneous emission has no effect on an atom's momentum, whereas absorption from one directional laser field supplies momentum in only one direction. These microscopic momentum exchanges will average on a macroscopic timescale to what will appear as a force.

Though it would be unrewarding to exhibit in full detail, one can derive the optical Bloch equations beginning with $i\hbar\frac{d\rho}{dt} = [H, \rho]$ and Eq. 1.9. From these the total scattering rate γ_p of the light field from atoms can be recovered,

$$\gamma_p = (1/\tau)\rho_{ee} \tag{3.1}$$

If one works through the optical Bloch equations, one can recover a clear expression for ρ_{ee}. The result is shown below. Let $s_0 = \frac{I}{I_s}$ be the on-resonance saturation parameter where I_s is the saturation intensity and I is the intensity of the light field, γ[b] the decay rate of the excited state and δ the detuning. This gives the scattering rate as[9]

$$\gamma_p = \frac{s_0\gamma/2}{1 + s_0 + (2\delta/\gamma)^2}, \tag{3.2}$$

which is proportional to the excited state population and is thus a Lorentzian as a function of detuning.

The scattering rate indicates the frequency of events that can impart a

[b] We are not considering broadening or Doppler effects here and will use γ rather than β.

force. Working from Eq. 3.2,

$$Force = (\text{momentum-exchanged}) \cdot (\text{frequency-of-change})$$

$$F_{\text{scat}} = \hbar k \gamma_p \tag{3.3}$$

$$= \frac{\hbar k s_0 \gamma/2}{1 + s_0 + (2\delta/\gamma)^2} \tag{3.4}$$

Using γ_p here folds in the light field properties as they affect the atom. Again, the excited state population is limited to 1/2, thus the scattering force has an upper limit, $F_{scat-max} = \hbar k \gamma/2$. This limit makes sense when considering stimulated emission. Consider an atom that has absorbed light traveling in the $\hat{x}$ direction. If the light is sufficiently intense, the light field can cause stimulated emission into the $\hat{x}$ direction: this will yield a brief change in velocity but no net momentum change.

3.1.1 Doppler Cooling - Optical Molasses

The scattering force can now be used to engineer a light field that opposes an atom's motion in 3D. For this purpose, consider six laser beams in counter-propagating pairs. With the appropriate (negative or red) detuning of the light fields, the Doppler effect will reduce absorption along the direction of propagation while enhancing it against the direction of propagation. Using Eq. 3.4 and $\omega_D = -\Gamma\delta = \vec{k} \cdot \vec{v}$ as the Doppler shift, we can reach an approximation[c] of $\vec{F}_{OM}(\vec{v})$ [9]:

[c] Treating the Doppler shift as small after the fractions of F_+ and F_- are joined, i.e. dropping it from the final denominator.

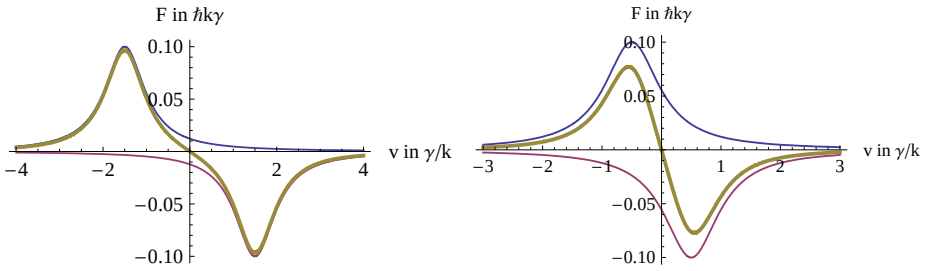

(a) $s_0 = 0.25, \delta = -1.5$ (b) $s_0 = 0.25, \delta = -0.5$

Figure 3.1: Plots of optical molasses force showing both beams separately and added. Note that with large detuning (left), capture velocity can be extended without total sacrifice of low-velocity force.

$$\begin{aligned}
\vec{F}_{\text{scat},\pm} &= \pm\frac{\hbar\vec{k}\gamma}{2}\frac{s_0}{1+s_0+\left[2(\delta\mp|\omega_D|)/\gamma\right]^2} \\
\Rightarrow \vec{F}_{OM}(\vec{v}) &= \vec{F}_+ + \vec{F}_- \\
\vec{F}_{OM}(\vec{v}) &\simeq -\frac{8\hbar\delta\Gamma k^2}{\gamma}\frac{s_0}{\left(1+s_0+(2\delta/\gamma)^2\right)^2}\cdot\vec{v} = -\eta_{fric}\vec{v}
\end{aligned} \tag{3.5}$$

Here we keep track of ω_D just long enough to reorganize the fractions, then make the reasonable approximation that $\omega_D/\gamma \simeq 0$. This is a friction[d] force; as shown in Fig. 3.1b, the linear variation with respect to small velocities leads to the approximation that η_{fric} is a constant.

A key detail here is that there is no position dependence: atoms are always entering and leaving the trapping volume. The intersection region for the cooling beams slows atomic movement, as if it were viscous. This leads to the term 'optical molasses.'

[d]This momentum-exchange-based friction force is distinct from the dephasing friction of Sec. 2.1.2.

3.1.2 Temperature

The 'temperature' for very low-density atomic collections can be defined as the average kinetic energy of these atoms; $\frac{1}{2}k_BT =< E_{kin} >$. Thermodynamics balks at the concept of temperatures of zero for a variety of reasons. Limits to cooling processes are clearly expected.

In optical molasses, the forces that 'cool' atoms are based purely on light. Force exchange is based on scattering events; light is directionally absorbed but randomly emitted. These random emissions may average to zero but the momentum exchange is conducted in units of $\hbar\vec{k}$ where $\vec{k}$ is the photon wave vector; the $v_{root-mean-square}$ of these exchanges is very much not zero[9]. The consequence is random motion in the molasses region.

To analyze[e] the heating effect from these exchanges, the frequencies of light absorbed and emitted must be considered;

$$\omega_{abs} = \omega_0 + \vec{k}_{abs} \cdot \vec{v} + E_r/\hbar$$
$$\omega_{em} = \omega_0 + \underbrace{\cancel{\vec{k}_{em} \cdot \vec{v'}}}_{\text{Avg's to zero}} - E_r/\hbar$$

Here ω_0 is the resonance frequency of the transition in consideration, $\vec{k}_{abs} = \omega_{abs}/c, \vec{k}_{em} = \omega_{em}/c$, $\vec{v}$ and $\vec{v'}$ are the velocities before and after absorption. Relativistic terms in the above equations have been omitted, as the velocities are extremely low and relativistic frequency shifts are negligible. $E_r = p^2/2M = (\hbar k)^2/2M = \hbar\omega_r$ is the recoil energy, the cause of the heating effect. We find the change in energy from an absorbed to an emitted photon

[e] This discussion of Doppler temperature taken from [9, 10]

easily,

$$\Delta E = \hbar(\omega_{em} - \omega_{abs}) = -\hbar\vec{k}_{abs} \cdot \vec{v} - 2E_r \tag{3.6}$$

In order for cooling to occur, this quantity must be positive; the photons must carry away energy. Note that because the wave-vector and the velocity have direction, cooling can occur. The recoil energy is unavoidable and thus leads to a heating rate proportional to the magnitude of this recoil and the frequency of scattering events from both directional beams:

$$\text{Recoil heating} = 2\gamma_p \times 2E_r = 4\gamma_p \frac{(\hbar k)^2}{2M} \tag{3.7}$$

Setting this heating rate equal to the cooling rate derived from Eq. 3.5 ($\vec{F}_{cool} \cdot \vec{v}$) and a little algebra results in

$$\frac{1}{2}Mv^2 = \frac{\hbar\gamma}{8} \frac{(1/2)Mv^2}{\frac{\gamma}{2\delta} + \frac{2\delta}{\gamma}} \tag{3.8}$$

The minimum energy is dependent on the detuning. Appropriately minimizing the energy results in the Doppler temperature:

$$T_D = \hbar\gamma/2k_B \tag{3.9}$$

3.1.3 Sub-Doppler Cooling

Experimentalists demonstrated optical molasses in 1985[11], but by 1988 realized a bit more had been achieved: the resultant temperature was significantly

lower than predicted by theory[21]. The source was eventually found to be a combination of complex level structure and beam interference effects.

If we return to Eqn. 1.8, we can look at the Hamiltonian matrix of the system. Please note that the following describes perturbations on the ground and excited energy levels. Recall, $\chi = \chi_{12} \propto$ electric field (Eq. 1.7) and $\Delta =$ laser detuning.

$$\mathcal{H} = \frac{\hbar}{2}\begin{pmatrix} 0 & \chi \\ \chi & \Delta \end{pmatrix}$$

If we diagonalize, we find energy shifts of

$$Energy_{excited(2)} = \frac{\hbar}{2}(-\Delta/2 - \chi)$$
$$Energy_{ground(1)} = \frac{\hbar}{2}(-\Delta/2 + \chi)$$

Each of these level shifts in practice is more sophisticated; Clebsch-Gordon coefficients are required, which depend on light-field polarization as well as magnetic quantum numbers.[9] Nonetheless, it is clear there are level-shifts dependant on electric field intensity; that is, the Stark shift.

Let us examine the case of two linearly polarized beams with orthogonal polarization angles. The interference of these beams results in polarization gradients; light alternates on a quarter-wavelength scale between σ^+, linear($+45^o$), σ^- and linear(-45^o). The Stark shift of the ground states causes them to vary, as shown in 3.2. As the level shifts depend on the field intensity and thus the instantaneous polarization, the sublevels involved in cooling will interchange

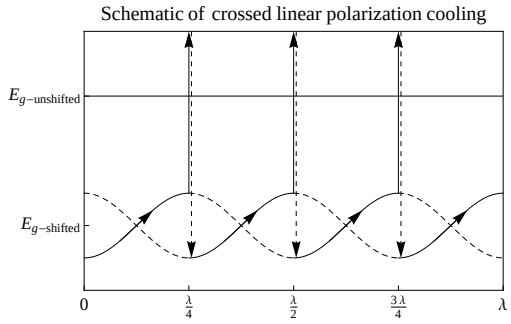

Figure 3.2: Schematic of polarization gradient cooling, with two orthogonal linear beams. The solid path is an ideal case of cooling, the atom loosing the maximum energy every quarter-wavelength. The energy lost is accounted for in the frequency of emitted light. This effect occurs alongside Doppler cooling, maintaining the directionality indicated by the arrows on the solid level.

repeatedly. Absorbing from the light field will increase angular momentum whereas spontaneous emission will on average have no effect on the angular momentum. The net result is pumping from the higher sublevel into the lower sublevel, thus loosing energy.[9] Note that the ground state cannot be significantly Zeeman shifted, as this will reduce the amount of cooling until it cancels out the effect completely.

This is Sisyphus cooling, named so because cooled atoms must climb the potential induced by polarization gradients again and again. This accounts for the experimental observation of lower-than-expected temperatures[21]. While the example here was for linear polarized beams, roughly the same cooling effects for opposed circular polarization schemes are observed. The mechanism is understood in a somewhat different way, but the practical differences are small and further discussion is unnecessary.

3.2 Magneto-Optical Trapping Theory

The forces described above have no position dependence. They can cool atoms but there is no trapping; atoms are always diffusing in and out of the the cooling region. In fact, it is quite possible to have different thermal distributions in different dimensions in optical molasses. By using a magnetic field it is possible to introduce a position dependence to the forces involved in these slowing processes and cause accumulation and interaction of atoms in such a geometry.

3.2.1 One-Dimensional Model

Let us develop a simple one-dimensional model of a magneto-optical trap (MOT). Take an atom with spin zero in the ground state (this reduces the complexity of multiple magnetic ground states) and spin one in the excited state. Take a linearly increasing magnetic field $\vec{B}$ with zero at the origin; the magnitude near the origin

$$B(\vec{x}) \equiv b\ \vec{x}.$$

with b the slope of the magnetic field. Two counter-propagating beams of equal helicity[22] (thus opposite circular polarization) are used, as shown in Fig. 3.3. These beams are red-detuned. When the atom encounters a significant Zeeman shift, this beam will be brought into resonance with a magnetic sublevel and the atom will experience a force.

The energy shift due to the Zeeman effect is dependent on the magnetic

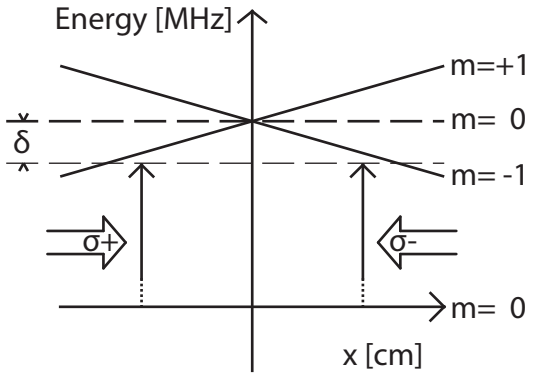

Figure 3.3: One dimensional cartoon model of a MOT. Opposing circularly polarized beams (opposite circular polarization, identical helicity) cycle light between the ground state and the lowest magnetic state. Consider the x-axis as m=0

sublevel, m_F, the field strength $\vec{B}$, and the Lande g-factors of the relevant levels, g_F. The Bohr magneton is $\mu_B = h \cdot 1.399\text{MHz/G}$.

$$\begin{aligned} \Delta E_{Zeeman} &= \mu_B g_F m_F |\vec{B}| \\ \Delta E_Z &= \mu_B g_F m_F b |\vec{x}| \end{aligned} \tag{3.10}$$

Only the light interacting with the atom is relevant; a different sublevel will be used from one side to the other of the field minimum. This will cancel out the negative direction of the field, thus we will use the absolute value of position. The ground and excited state will both be affected by the Zeeman shift, complicating the picture somewhat. Here the subscripts refer to the

ground and excited states,

$$\hbar \cdot \delta_Z(x) = \mu_B(g_e m_e - g_g m_g) b|x| \tag{3.11}$$

$$\delta_Z(x) = \tilde{\mu}|x| \tag{3.12}$$

To find the total force in a MOT, we need to consider Doppler cooling as well as the contribution from the above term. To do this, we will use the detuning observed by the atom as determined by the laser detuning, atom velocity and position (thus magnetic field)

$$\delta_\pm(\vec{v}, x) = \delta \mp \vec{k} \cdot \vec{v} \pm \tilde{\mu}|x|) \tag{3.13}$$

The same scattering force equation (Eq. 3.4) will be used to start this calculation;

$$\vec{F}_\pm = \pm \frac{\hbar k s_0 \gamma/2}{1 + s_0 + (\frac{2}{\gamma}\delta_\pm)^2}$$

Obviously the detuning and thus the force will be different for the different beams. This is embodied in the detuning.

$$\begin{aligned}\vec{F}_{MOT} =& \vec{F}_+ + \vec{F}_- \\ =& \frac{\hbar\vec{k}\gamma}{2} s_0 \left(\frac{1}{1 + s_0 + (\frac{2}{\gamma}(\delta - \vec{k} \cdot \vec{v} + \tilde{\mu}|x|))} + \frac{1}{1 + s_0 + (\frac{2}{\gamma}(\delta + \vec{k} \cdot \vec{v} - \tilde{\mu}|x|))}\right)\end{aligned}$$

Executing the same approximation procedure used previously, e.g. rearranging the fractions and then assuming that the detuning is small and thus that we

are close to the center of the trap, the following result is obtained

$$\vec{F}_{MOT} = -\eta_{fric}\vec{v} - \tilde{\mu}_{trap}|x| \tag{3.14}$$

where $\tilde{\mu}_{trap} \equiv \frac{\tilde{\mu}}{k} \times \eta_{fric}$ (see Ref. [23] for derivations of this and above). The above expression is a restoring force with damping. Overdamped motion is typical in such a trap.

3.2.2 Three-Dimensional Model

A three dimensional MOT is significantly more complicated than the above model. Two beams for each axis must meet in the same region where a controlled magnetic field can be generated. This field is usually generated by a pair of anti-Helmholtz coils (large orange/copper coils sketched in Fig. 3.4 and shown in Fig. 4.1).

Many factors serve to complicate a real-world MOT. There are Zeeman shifts of both the ground and the excited state, requiring a calculation of Eq. 3.10 for each. Further complicating matters, an atom's velocity as used in the Doppler shift of Eq. 2.4 may not be parallel to any beam. Finally, as an atom moves around the trap, the magnetic field changes direction and intensity in a well-known but still complex way.

Beyond the subtleties of three dimensions, hyperfine structure begins to play a role. In Fig. 3.5 we see the transition that will serve as primary means of momentum transfer, referred to as the cycling transition. Given the complex level structure, occasionally an atom will decay to the wrong ground state (F=1) and the repump light will move it to a state where it can decay back

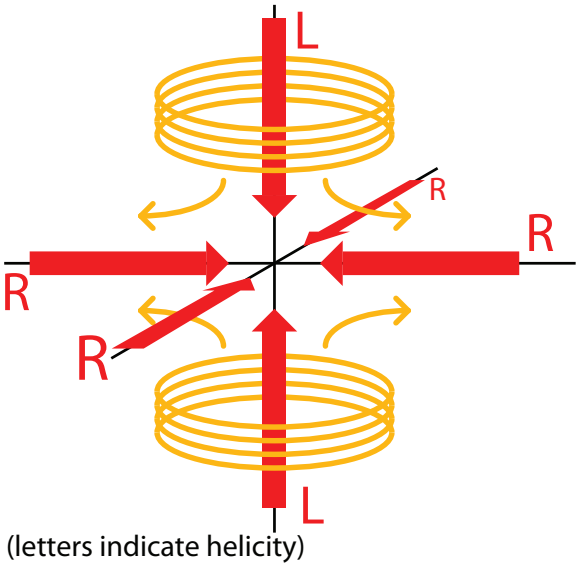

Figure 3.4: Primary MOT coils shown as orange loops, field direction indicated by same-color arrows. The coils are in an anti-helmholtz configuration. MOT beams and their helicities indicated in red.

into the cycling transition. This light need not be very intense, nor come from all directions.

3.3 MOT Loading

When considering the loading behavior of a MOT, one reveals many interesting parameters. The number of atoms in a MOT is governed by a simple capture rate[24] and two significant loss mechanisms[25]: collisions of cold atoms with hot background gas[f] and collisions of cold atoms with other cold atoms.

While a MOT is a trap for cold atoms, atoms must find their way into the trap. Two schemes are widely used for this purpose. One scheme cools the atoms by means of a Zeeman slower and then deposits them into a very

[f]It is reasonable to assume background gas is nearly all ^{87}Rb .

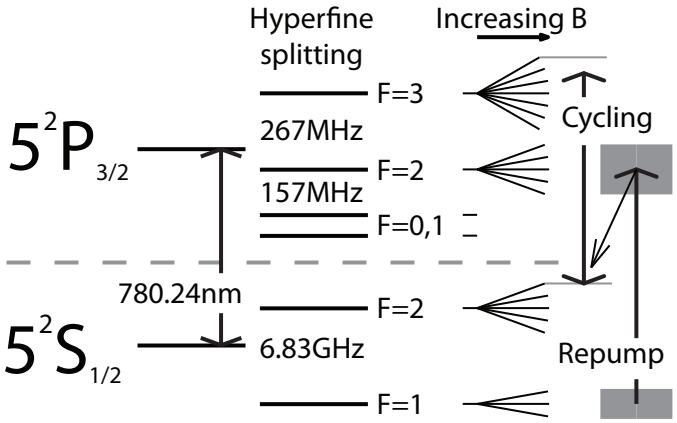

Figure 3.5: Shows the cycling and repump transitions for the ^{87}Rb MOT. Weak-field Zeeman splitting is schematically shown. Data from [16].

good vacuum where the MOT waits. If patient and willing to trap from the minuscule low-velocity fraction of the velocity distribution, one can trap in a reasonably good vacuum from background vapor. Each scheme has its advantages and disadvantages; our apparatus was designed to trap from background vapor.

3.3.1 Capture Velocity

A precise definition of the capture velocity of a MOT is difficult, as the asymmetrical nature of the trap geometry used in nearly all systems brings heavy emphasis to path dependence. One simplified approach to estimating this velocity relies heavily on the one-dimensional model illustrated in Fig. 3.3. Consider an atom on the left side of the MOT, being stopped by the beam originating on the right. At this point, the Doppler shift of the absorbed light works in concert with the Zeeman shift. The maximum allowed Doppler shift will set a limit on the velocity. Beyond this velocity, the radiation force

from the beam will become increasingly small. The shift between excited and ground state of ^{87}Rb is roughly 1.4 MHz/G. Assume a field of 20G, which yields a 28MHz shift. Added to this Zeeman shift (on the far-side of the beam that is performing the slowing) is the laser detuning (assume a typical value of 20MHz); we need a Doppler shift to match 48MHz. The transition frequency in question for rubidium is ∼384THz. Atoms must be going 37.5m/s to see a shift of 48MHz. Slower atoms will eventually find a weaker field, coming into resonance and being slowed.

The above result is within 20% of the following method. Ref. [23] gives v_c as the velocity of an atom stopped by half the maximum scattering force within the radius of the trap (values of $\simeq$ 2cm are reasonable). The maximum scattering acceleration (recall 3.3) is given by $a \simeq \hbar\gamma_{linewidth}/4m$.

$$\begin{aligned} v_c =& \sqrt{2ar} \\ =& 47.5\text{m/s} \end{aligned} \tag{3.15}$$

Integrating the Maxwell-Boltzmann distribution properly, one finds that only a fraction of a percent[g] of the available atoms are being trapped. The result is experimentally determined loading times of approximately 10 seconds.

3.3.2 Capture Rate

To calculate the capture rate in a transparent way one needs the surface area of the trapping volume (or a reasonably good estimate) and the capture velocity

[g]Integrating Eq. 2.5 from zero to 37.5m/s, we find only 0.28% of atoms are being captured at any given moment.

of the trap. If an approximately spherical trapping geometry is assumed, the capture rate R will be found[25] by integrating the velocity distrubtion

$$R = \pi r^2 \int_0^{v_c} v S_{3D}(v) \mathrm{d}v. \tag{3.16}$$

3.3.3 Loss Mechanisms

There are two significant loss mechanisms in a MOT, intra- and extra-MOT collisions; let $N(t)$ be the number of trapped atoms, R the capture rate, Γ the loss rate due to hot background gas and β the loss rate due to cold intra-MOT collisions. R can be calculated[24] by considering the cross section, flux and number of atoms in the distribution below v_c.

$$\frac{dN}{dt} = R - \Gamma_{coll} N(t) - \beta N(t) \tag{3.17}$$

$$R = \frac{n_{bg}}{2} V^{2/3} {v_c}^4 \sqrt{\frac{m}{2kT}}^3 \tag{3.18}$$

$$\Gamma_{coll} = n_{bg} \sigma_{bg} \sqrt{\frac{8 k_B T}{\pi m_{bg}}} = n_{bg} \sigma_{bg} v_{bg} \tag{3.19}$$

Here n_{bg} is the density of the background gas, σ_{bg} the cross section and V the trapping volume. A rigorous calculation of Γ_{coll} involves careful consideration of the energy of the background gas relative to the escape energy required for an atom in the trap. Given that the trap depth is very small compared to the energy of the hot background gas, it is reasonable to neglect such details. In fact, since most of the experimental parameters that vary from lab to lab are bound up in the trap and not the room temperature background gas, a comparison of empirical values find them reasonably similar.

Once captured, these atoms will only escape due to collisions with background gas, which is already at a very low pressure. Eventually a balance is obtained between background pressure, detuning and total loading rate. With the settings stated here and a moderately high background pressure (for the capabilities of this system), loading times on the scale of a few seconds are routine.

3.3.4 Loading Dynamics

We now have equations for the loading rates as well as the maximum number of trapped atoms. Taking N as the population in the MOT, R as the loading rate and G as the loss rate due to scattering from hot background gas,

$$\begin{aligned} \dot{N} =& R - GN \\ N =& \frac{R}{G}(1 - e^{-tG}) \end{aligned} \tag{3.20}$$

High background pressure yields high loading rates. The steady state atom number, $N = \frac{R}{G}$ is independent of pressure. In this steady state condition, it is clear that loading and loss rates are equal. Also, for other forms of trapping (i.e. magnetic trap for transport, dipole trap for experiments with no field) high background pressure means very short lifetimes. This will play into the design parameters of the vacuum system in the next chapter.

Chapter 4

Implementation

The theory of the previous chapters is at best an exciting experimental challenge. High current for carefully constructed magnetic fields, water cooling, delicate optics, two regimes of extremely good vacuum and translation of cold clouds between those regimes all come together in the same dense volume of experimental space. The end result is a trapped atomic gas with temperatures below one milikelvin. The details of these systems, choices made in their construction and techniques used to build them are covered.

4.1 Laser System

We'll begin with the full laser systems as shown in Fig. 4.2. To the left of each laser are the spectroscopy systems, described in detail in chapter two. From the theory set down in chapter one, it is apparent that a variety of frequencies will be required for magneto-optical trapping as well as the detection of any trapped atoms. As such, two lasers are used, along with many frequency-

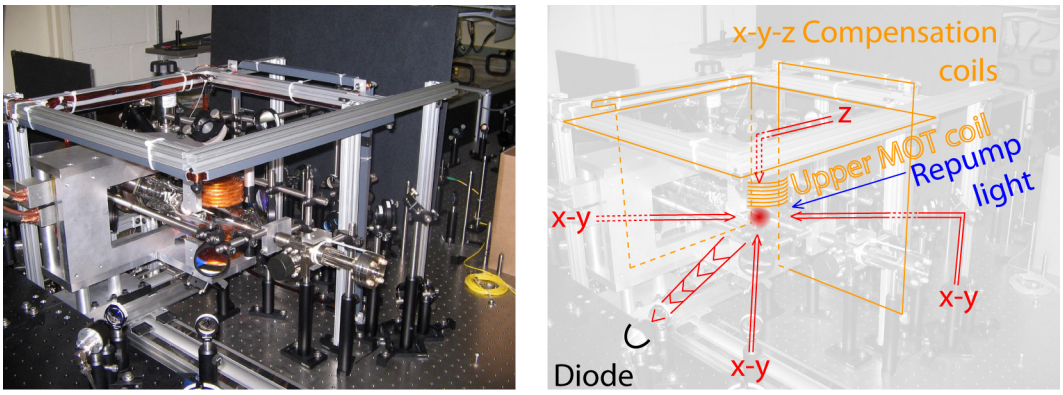

Figure 4.1: Overview of MOT-side, before construction of BEC-side. Several components are marked in the right pane.

shifting components.

For the cycling transition light, a Sacher TEC 300[a] was used, with 1000mW of available output power. As mentioned in the previous chapter, this is an extended cavity grating diode laser, with the grating in a Littrow and rear-face coupled design.

The laser used to repump atoms back into the cycling transition is a Toptica DL-100, with a lower output power and proven design.

Somewhat excessive mounting blocks were made for both lasers; several inches tall and made of solid aluminum, these were chosen to maximize stability. The optical table used was donated and had some irregularities in surface flatness. To avoid strain on the laser baseplates, each mounting block was kinematically mounted via clamps and ball-bearings to the optical table.

[a]The Tiger is one of the highest power single-stage diode lasers on the market, meaning there is no master-slave pair of diodes. As a result, the technology for these diodes seems to not be as mature as one would like. The decay-over-time for these diodes was unpredictable. Several diode failures were experienced. In addition, even with the best locking parameters, the frequency was observed to jitter by ±10MHz due to acoustic noise.

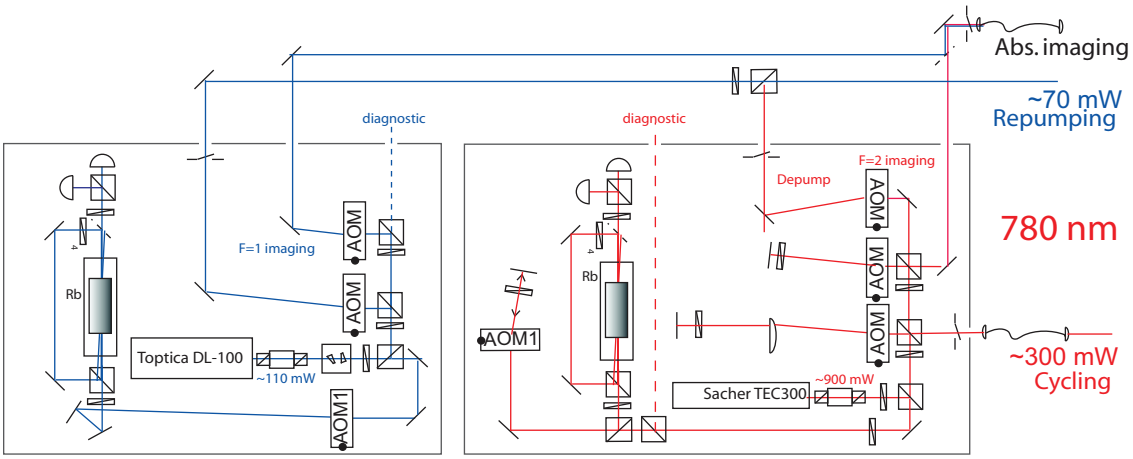

Figure 4.2: Overview of laser optics. A so-called 'cat-eye' construction was used for the cycling AOM to avoid translation of the beam during frequency sweeps.

4.1.1 Laser Optics

The optics systems for both lasers are motivated by power and frequency requirements. Each laser had an output power on the scale of that required by the system. Losses were minimized in a variety of ways.

The very first and most crucial element in both parts of the the system is an optical "diode". This is a one-way optical component that prevents accidental feedback from disrupting the mode characteristics of the laser cavity. These diodes are Faraday isolators[b] purchased from Linos Optics, specified to reduce return light by 40dB. While the Sacher also has a built-in 38dB isolator, another was needed. The Toptica laser did not ship with an isolator thus one was built in to our custom mounting block.

Many half-waveplate + polarizing-beamsplitter units are used; this allows

[b]This diode works via the the Faraday effect, induced by strong magnets around an optically active crystal. Polarizing optics are part of this device; the laser output is thus polarized.

easy variation of power distribution through the entire system.

Acousto-optic modulators (AOMs) drive nearly all branches of the system. In an AOM, RF radiation induces sound waves in a crystal. Light is Bragg-diffracted off of the sound waves, resulting in a frequency shift equivalent to that of the sound waves. All our AOMs were purchased from Isomet and operate at roughly 87MHz with $> 85\%$ efficiency. Separate branches of the systems are labeled according to frequency in Fig. 4.2. Each AOM frequency can vary from 60MHz to 92MHz, with reasonable efficiency in a smaller band around the required 80MHz. The scattering process is dependent on many factors including frequency and operates below $\approx$60MHz on the scale of 20% efficiency.

A small amount of light from each laser is sent to a scanning Fabry-Perot cavity. This yields information about the mode structure of the lasers. The signals from both lasers are mixed, but are clearly distinguishable on the oscilloscope readout. This allows for quick diagnosis of possible laser problems and easy assessment of stability (e.g. multi-mode or mode hopping).

The most important branch of the Sacher system handles the cycling transition. To begin with, all of the AOMs were tested for transmission. The highest efficiency AOM was used on the cycling branch. The AOM apertures were significantly smaller in the vertical dimension than the unmodified beam diameter emitted from the Sacher. Cylindrical lenses created a 1:1 telescope around the AOM (not shown in Fig. 4.2), focusing in the vertical direction. This allowed the beam to fit through the aperture of the AOM, while not affecting the optics of beam deflection. After the 1:1 telescope, a lens was set up with its focus set inside the AOM. The ray exiting this lens is then parallel to

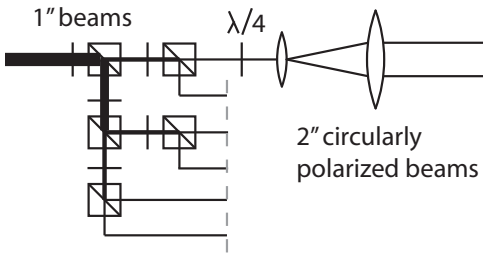

Figure 4.3: A schematic of the template for power distribution in the beams. The unlabeled waveplates are $\lambda/2$ to proportionally adjust power. Line thickness is roughly proportional to power.

the first ray entering this branch, no matter the frequency offset of the AOM. A $\lambda/4$ waveplate is included in this branch, resulting in a net 90^o rotation, allowing the return beam to pass through the polarizing beamsplitter. A tilted lens is introduced to adjust for the slight astigmatism of the beam (diodes are notorious for horrible output modes, due to their understandably rectangular structure). The light is sent into a single mode fiber to clean up the mode. The beam is then partially expanded and 1" beamsplitters are used to divide the beam (Fig. 4.3) into the necessary six orthogonal beams. The beams are then folded around the glass chamber (Optics on the far side of Fig. 4.1) and sent into final telescopes expanding to the 2" diameter of glass chamber.

4.1.2 MOT Optics

The organization behind the trapping optics was established in collaboration with R. Schiller and H. Ruf. A single-mode fiber connects the laser system (Fig. 4.2) to the beam distribution optics, Fig. 4.3. The beam is partially expanded first, then split into the necessary components and polarizations. The last stage is a $\lambda/4$ plate and the final 2" telescopes.

4.2 Vacuum System

The vacuum system was designed to be constructed in two parts, forming a magnetic-transporter type geometry[8]. The first part has a higher background pressure of ^{87}Rb for the sake of MOT loading times. A narrow connection to the second half of the system is maintained, keeping a high pressure differential. This second half is maintained at such low pressures that the only available measurement technique is based on trap lifetimes. This is where Bose-Einstein condensates are now created.

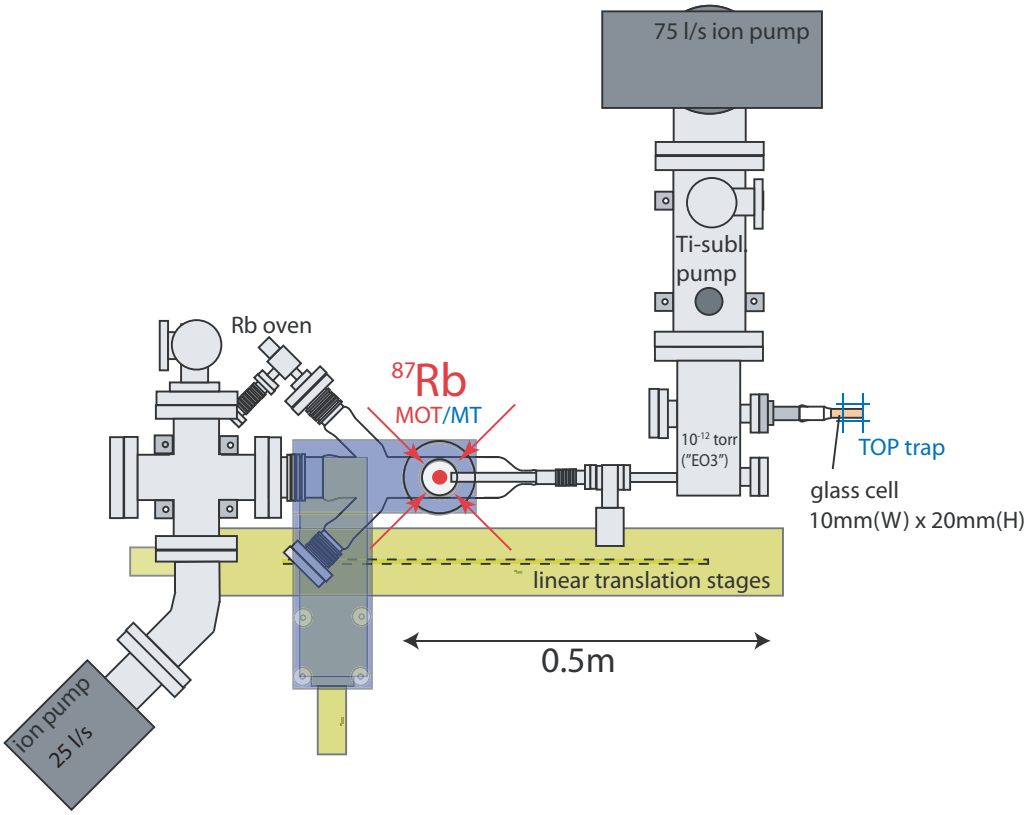

Figure 4.4: Schematic of completed machine, to scale. Optics not shown.

4.2.1 Design

The main component of the MOT side of the vacuum system is the trapping cell. Many ideas came together in the design of the MOT cell. Beam distortion from the glass surface is known to have little effect on the quality of the MOT[8]. Two angled ports (leaving optical access) into the glass cell were planned: one for a rubidium oven, the second for a vacuum gauge[c]. The large opening on the 'left' side of the machine allows for good pumping of the region. The large-diameter four-way intersection connecting the pump to the cell does decrease pump speed slightly; however, it allows for the pump-down port, vacuum gauge and a large flat (inexpensive) window that views the trapping region. This window is very convenient for imaging.

Expansion into a second vacuum system with significantly lower background pressure also put constraints on the system. The pressure regimes involved are all ballistic thus it is easy to geometrically induce a large pressure difference between segments of the system; a long narrow tube ("differential pumping tube") allows three orders of magnitude pressure differential between the two sides of the system. Rather than add the length of this differential pumping tube to the whole system, the small-aperture tube is fed into the trapping region. This reduces the travel required by atoms from one section of the system to the next. The optical access of the trapping region is maximized while travel time to lower pressure regions is minimized.

[c]Never implemented, considered unnecessary.

4.2.2 Pressure Regimes and Assembly

One of the requirements for the system is to maintain a minimum lifetime of one second in a magnetic-trap configuration. This requires the pressure to be lower than 10^{-8} torr in the first half of the system.

Three elements are key to maintaining low pressure and high loading rate. The first is all-metal seals. Aside from one valve mounted opposite the pump, all seals in the system are copper gasket, conflat seals. The second major component is the pump itself. A 75 L/s Varian StarCell[26] ion pump is used. The lifetime of these sealed, solid state pumps is dependent on the pressure in the system. At 10^{-7} torr, a lifetime of 10 years[26] is extremely reasonable. Pressures at the pump are expected to be two orders of magnitude lower. Note that the only pump in the MOT half of the system is an ion pump; the system is completely closed, removing any need for roughing pumps.

During assembly, a vast quantity of gloves and single-use KimWipes were used to ensure minimal contamination of inside surfaces. Washes of acetone and ethanol were used to clean all surfaces before assembly. Copper gaskets were set aside and used last if accidentally touched by anything but an unused KimWipe. While somewhat extreme in the level of paranoia (and generating an equally extreme mess during construction), these techniques produced a system that worked the first time. Given the time involved in construction and all that follows prior to a clear measure of system performance, this was justified.

The MOT side of the system was constructed first, with a gate valve and small window past this. The gate valve was brought to good vacuum with

the MOT system. Once a MOT was established and sufficient components were designed, manufactured, ordered and received, the gate valve was closed, window removed and the second half of the system was added.

4.2.3 Pumpdown and Bakeout

The initial pumpdown of the system was performed via a mechanical-backed turbopump. The turbopump used was borrowed from a neighboring lab; it was required for at most a week for each side[d]. As most water- and oil-soluble contaminants were removed during assembly, the major contributor to initial background pressure was residual water in the surfaces of the metal. To enhance pumping of this water, the entire system was wrapped in heating tape and aluminum foil during initial pumpdown.

Baking the water out of a vacuum system may be a 'low-tech' solution to the residual water problem; however, the heating must be precisely controlled and the pressure in the system must be monitored quite closely. The system is primarily made of steel and borosilicate glass with almost all of the junctions sealed via copper gaskets. The steel and glass are both rather poor conductors of heat. If only part of the system expands, the seals would be weakened. To avoid this the temperature was raised very slowly to $\sim$200°C over the course of several hours and measured at dozens of points, allowing a close eye to be kept on gradients throughout the system.

The pressure was monitored throughout the process, allowing us to estimate the level of remaining contaminants in the system. It was known that

[d]The second side was constructed and pumped down many months after extensive testing and experimentation conducted in the first side.

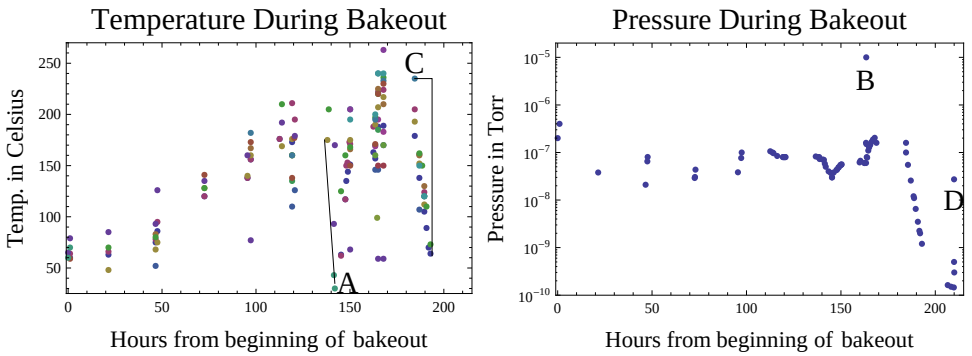

Figure 4.5: Plots of temperature and pressure during bakeout. Several points and lines are noted: (A) Line ending here indicates conclusion of controlled cooling of ^{87}Rb sample. At the end, several heaters were discovered accidentally unplugged. (B) A small gas blanket was on top of the ^{87}Rb vial. The turbopump was re-engaged and this was bled out, slowly. Shown here is the peak of the pressure during this bleed-out. (C) Cooldown of system begins. Horizontal line shown at C is 9 hours, vertical line is 170°C. (D) Some valves adjusted, pressure spiked but recovered. Final values reached roughly 10^{-10} torr.

(roughly) the pressure would drop one order of magnitude per 50°C. This estimate gave us a feel when the system had remained at high temperature long enough and could be slowly cooled off.

4.3 Transport

Before the results on magneto-optical trapping are presented, I will discuss a few components for which I did some calculations and optimizations. In the experiment, after a MOT has been prepared, the atoms are transported into an evaporation chamber (glass cell) using a mechanically translated pair of coils (which happen to be the same as the MOT coils). This transport is accomplished in a purely magnetic trap. While trapping monopoles is impossible, trapping dipoles in electrostatic fields is allowable.[27] The magnetic states of

our atoms interact with the applied magnetic field. However, these magnetic states can be up or down with respect to the quantization according to the applied field; there are trapped and anti-trapped states. The flipping of one state into the other can occur at the field zero in the center of the trap, termed Majorana losses. A larger fraction of atoms in a colder cloud will cross the zero more frequently than in a warmer one, leading to more losses. The more brief the time in the trap, the fewer the losses. This mandates rapid transport.

The mechanical translator consists of a pair of Parker-Daedal 404XR ballscrew translation stages, one 60cm long and one 10cm long. See Fig. 4.6 for an overview of the system. The stages were purchased as part of a total motion control system which included servo motors, drivers and a controller to execute programmed motion.

The translation stages are mounted semi-kinematically. The stage is sensitive to flexing of its mounted surface (decays bearing lifetime significantly) and a small increment in height was required, thus four gauge blocks were purchased and placed in roughly even intervals under the lower stage as flat surfaces. Eight points of pressure on the stage were established. The table on which the system was constructed was newly purchased upon establishment of the lab in 2005, thus surface flaws of any significance are highly unlikely.

The entire motion control system, once satisfactorily programmed, is operated by one low-to-high edge trigger, even during startup following power loss.

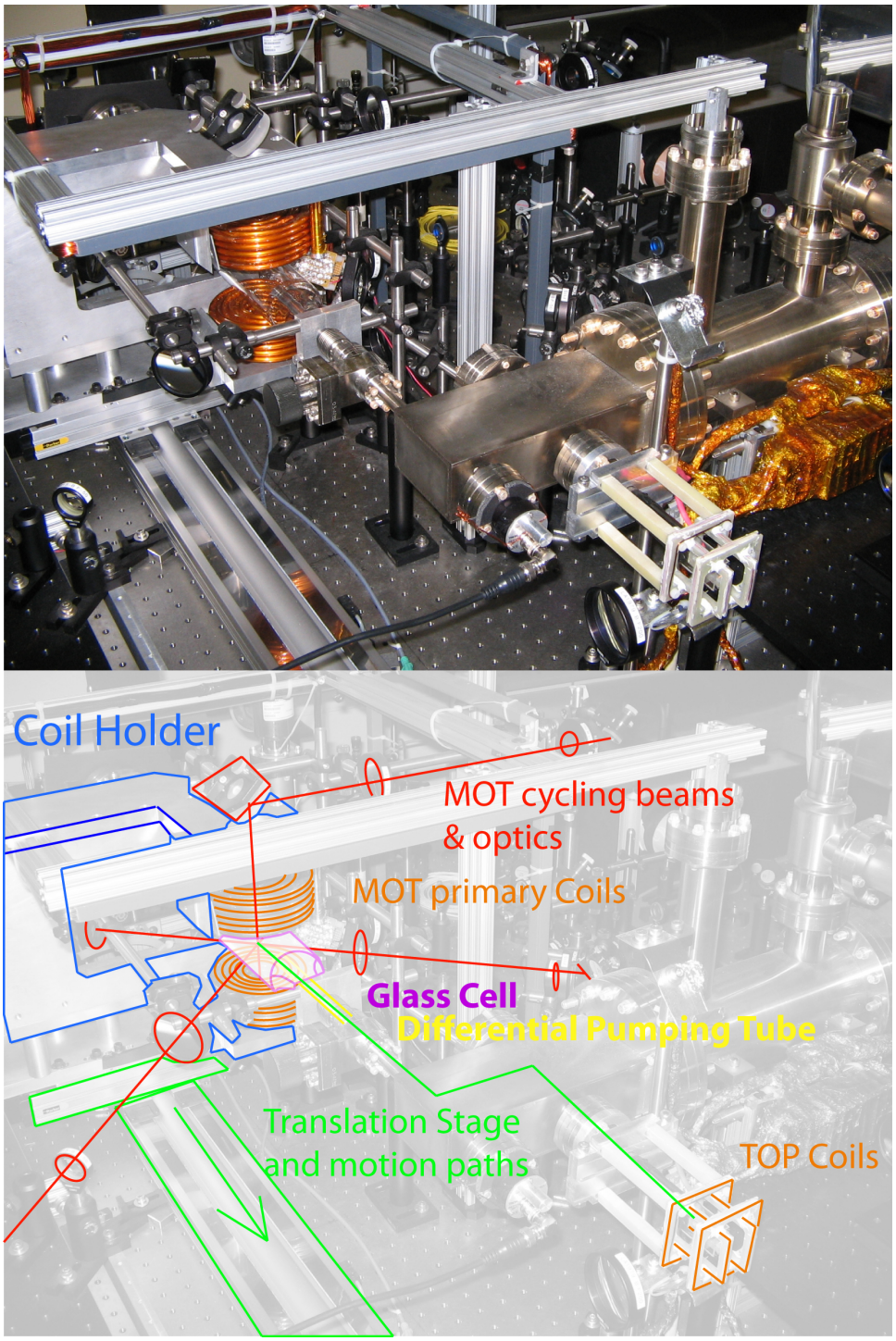

Figure 4.6: MOT and TOP coils shown. MOT coils attached around glass cell in upper left. TOP coils shown with white epoxy-fiberglass composite framework in the bottom right. Total length of the lower stage is 60cm.

4.3.1 Load Calculations

The lifetime of the translation stages was specified as expected travel-till-failure, dependent on the load characteristics. Force on the four corners of each platform as well as any acceleration torque is calculated and compared to tables to determine the lifetime of the system.

The translation stages have four support points to the track in which they travel. Each of these supports have a bearing lifetime. The array of all component masses (MOT coils, mass of their cooling water, coil holder, force due to power supply cable drag) and distances in the coordinate system of each translation carriage were calculated and set up in Mathematica to allow for easy lifetime estimates as several different coil-holder designs were considered. After deciding on a reasonable coil-holder configuration, it was found that the stages were expected to outperform the scientific relevance of the system by many years, even if run continuously at extremely high acceleration.

4.3.2 Electronics and Failsafe Programming

The electronics and motors driving the translation stages are quite intricate. There are three layers to the control system; the motors, the drivers (power the motors while managing the feedback loop) and the controller which issues commands to the drivers.

The servo motors can resolve and hold distances on the scale of individual counts, an internal unit of measure of which there are 4096 per revolution. The ballscrew drives are set such that one revolution is one cm, resulting in $2.4\mu m$ per count. The controller is capable of setting many of the detailed parameters

of the servo feedback loop, allowing extreme customization of motion. The scripting language that runs the controller has extensive functions allowing complex motions.

The translation path for the MOT coils is shown in Fig. 4.6; first is a long stretch, out of the 'high' pressure region. Next is a jog around a corner, escaping any ballistic trajectories exiting that region. While this motion path is somewhat elementary, it is still crucial to use controller-level interlocks to avoid crushing delicate parts of the system. Motion programs are always very carefully constructed, but perfection is impossible. The control programs are written with an failsafe command that, when triggered, will stop all motion (velocity to zero) immediately and shut down the servo feedback loop. Structural aluminum guard rails (see Fig. 4.7) are secured to the underside of a well-mounted breadboard, mimicking the configuration of collision points of the coil holder with the machine. A steel rod is attached to the coil holder for restraint; if a catastrophic motion is attempted, this rod will collide first with the structural aluminum. This rod is wound with a wire connected to the controller which supplies a positive voltage. Upon collision of rod to the aluminum rails, the wire will be brought to ground and will trigger the failsafe command, halting all motion. If the controller failsafe command fails, the structural aluminum will restrain the system. The motors will automatically shut down after a short time if the stages are physically restrained.

A handful of program adjustments have triggered the software failsafe. In two instances known to the author, the mechanical restraint system was necessary[e]. No catastrophic translation failures have damaged the machine or

[e]These events were during early stages of translation stage setup.

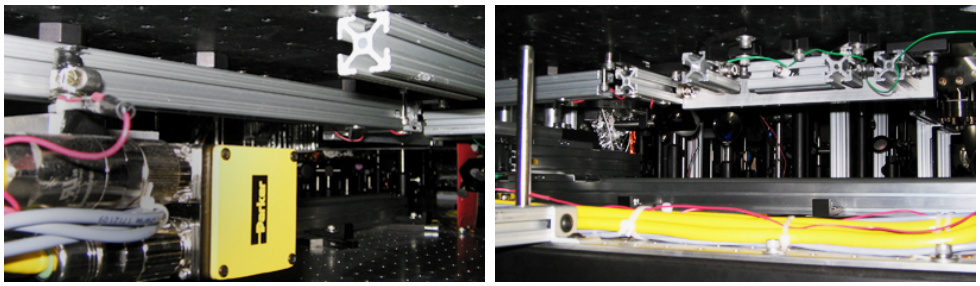

Figure 4.7: In the left we see the yellow servo motor housing and the relatively large power adaptors which are bracketing the sensor cables. The red lead is the control wire, attached to the steel pin. The extruded aluminum bars are secured to a breadboard segment and are held at ground with green wires shown on the right. Where applicable, the motion path of the control pin is bracketed on two sides.

the stage in any way.

4.3.3 Control Programming

The stages were shipped with three sensors each, designed to trigger when a tab on the carriage of the stage passed by. Given that power failures may occur, calibration of our translation coordinates must not be arbitrary or dependant on volatile memory. To accomplish repeatable and safe recalibration, an initialization routine was written.

On hardware reset, the encoders register a position of $(0, 0)$. However, if the program loop is terminated and restarted (when motion control parameters are adjusted), the encoder position is not changed. The calibrated origin of the coordinate system was chosen in the middle of the motion path, a place where the stage would never come to rest during normal use. Thus, if the program starts at the origin (as in the case of a power failure), the initialization routine is activated, preventing motion until coordinates are verified.

Recalibration begins with a shutdown of the servo loop, allowing (and requiring) a user to manually shift the stage to where one of the position sensors will trigger. When the position sensor triggers, the servo loop is activated thus freezing the stage in place. The system then waits for the user to trigger the single control line. At this point, the drive (slowly) scans for the edges of the lower stage's position sensor. On finding these edges, the lower stage's coordinates are set. This sensor is located where the upper stage can move in full range. The system then scans for the edges of the upper stage's position sensor. Once set, the stage returns to the MOT position and enters into the 'run' loop.

The run loop is simple: on trigger it moves forwards to the BEC position and waits, the next trigger returns it to the MOT position. A small scrap of Mathematica code was written to calculate the appropriate timing, acceleration and velocity values. The motion parameters can be quickly adjusted in this way.

4.4 Magnetic Coils

Several sets of magnetic coils are used for both the MOT and the BEC apparatus. The primary set used for the MOT is attached to a translation stage and is also used in the BEC portion of the system.

The primary MOT coils are set up in an anti-Helmholtz configuration (See Fig. 3.4) and serve three purposes. First, as a source for the low-level field required for the MOT. Secondly, as a pure magnetic trap used to hold the atoms for transport to the BEC side of the machine. Finally, as part of the

moving-coil time-orbiting-potential trap (McTOP trap). An approximate form of the MOT coil field (valid only near the origin) is given below with B'_q as the slope of the field.

$$\vec{B}(\vec{r}) \propto -2B'_q z\hat{z} + B'_q x\hat{x} + B'_q \hat{y} \tag{4.1}$$

4.4.1 Calculations

Several key constraints went into the first generation of coils; the amount of heat that could be dissipated via available water cooling, the cost of materials[f] and the available power supplies.

When it was decided that some variant of a TOP trap would be used, there was a need for more detailed simulations. The author wrote a set of Mathematica routines to calculate these fields. Several models for this code had been attempted but were too slow in calculation times. The calculation scheme used is built around an effective implementation of the Biot-Savart law;

$$d\vec{B} = \frac{\mu_0}{4\pi}\frac{\vec{dl} \times \hat{r}}{r^2} \tag{4.2}$$

and is outlined in Fig. 4.8. There are two key features: first it calculates the field only for a small grid of specified points, saving calculation time; second it will break a wire segment into smaller pieces according to a scale parameter.

The coils are supplied to the code in the form of lists of points. Indeed,

[f]Some groups have used square cross-section coils in order to gain performance; this typically requires a special distributor or a 500lb order directly from the supplier.

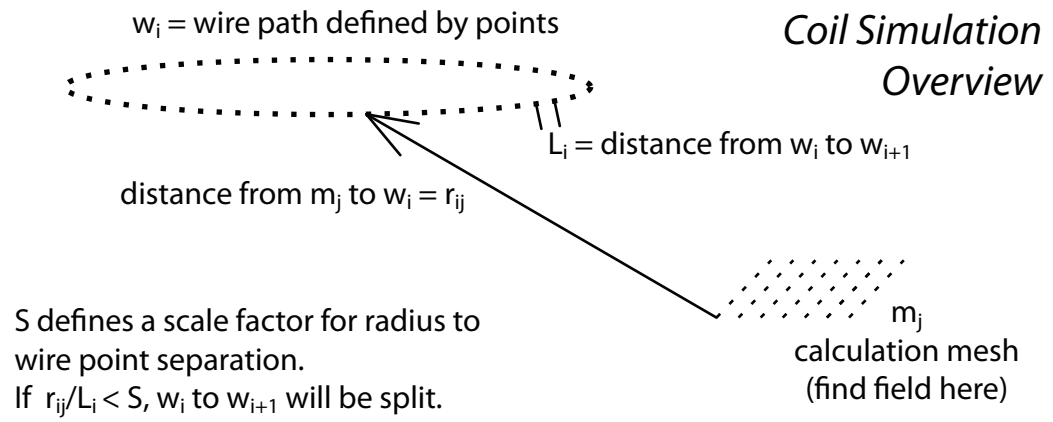

Figure 4.8: An outline for the structure of the simulation code. Two lists of points are required, for the wire generating the field and for the points where the field information is required. The code scales according to the factor S, attempting to increase efficiency without sacrificing accuracy; it is assumed that the wire points sufficiently define wire path. A simple Biot-Savart law is used.

'building' the coils in this way took a non-trivial amount of time. Code was used to build them from pieces of functions, so the number of points could be specified (e.g. the precision could be adjusted). Point density could be increased where the wire bent more or was close to calculation regions, whereas it could decrease for more straight runs or for regions far away.

Each pair of points is treated by the code as portions of straight wire (hereafter referred to as coil-lines). These are further broken down into sub-segments such that the nearest sub-segment has a given ratio to the distance from the calculation points. Coil-lines very far from the calculation points have fewer sub-segments, where coil-lines nearer to calculation points have many more sub-segments. The ratio of sub-segment length to calculation distance can be adjusted to increase or decrease accuracy: poor accuracy leads to short calculation times, while high accuracy leads to somewhat increased calculation

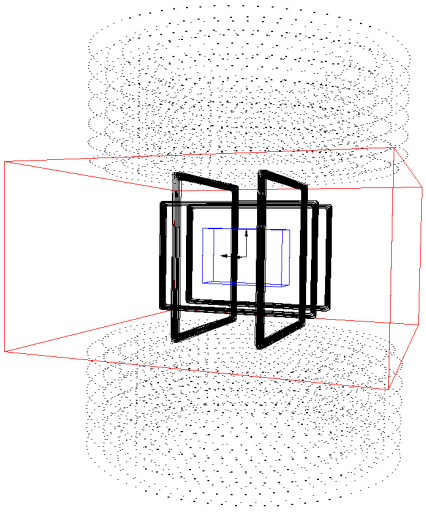

Figure 4.9: Calculation framework for magnetic simulation code. The largest box is the volume MOT coils cannot impinge upon. The smallest box is the final glass cell. The large arrays of dots define the MOT coils. The striated dark loops are the final magnetic trap. On the scale of this image, simulations were carried for a volume of space about the size of a period.

times.

These simulations allowed us to verify the details of all the sets of coils, as well as their required precision in manufacture and assembly.

The nature of the TOP trap as a simple bias field applied to the quadrupole field lent itself to an easy method of simulation. The fields of each separate coil were calculated and superimposed, with the TOP coils having modulations of sine and cosine functions as would be implemented with electronics.

4.4.2 Design

The parameters that dictated the very first primary MOT coil design are heat, current flow and cost. The initial power supplies were bought at huge discount and were intended to give us a start rather than serve for the life of the system.

Also, the purpose of the primary MOT coils was expected to (and did) change during the system's development. A small infrastructure was progressively developed for the generation of MOT coils. At least four sets of MOT coils were created, with major participation by the author for all.

A variety of shapes were considered for the TOP coils; the simplicity of rectangular coils eventually won. The key feature of Helmholtz coils is the vanishing curvature in a large region between them. D. Pertot worked out the proper separation of two rectangular coils (dependent on the ratio of width and height) necessary to zero field curvature at the center of the coils. Two interlocking pairs of rectangles were chosen in the final version and tested extensively with the simulation code.

4.4.3 Construction

While the applied magnetic field intended to generate the MOT is significantly stronger than the Earth's field outside of the trapping region, the MOT is not the only trapping phase. In the optical molasses phase, the field will be turned off. If there is a residual magnetic field due to the Earth, the beam intensity will need to be adjusted to offset the Zeeman effect such that there is no average velocity in the cloud of atoms once released (or transferred to another trap). Compensation coils designed for low optical occlusion are oriented on three orthogonal axes[g]. When the MOT field is reduced, the uncompensated zero of the superposition of Earth and MOT fields will move, allowing for an easy diagnostic to calibrate the compensation field.

[g]Helmholtz pairs are typically used. However, the region that requires compensation is very small. In our system only three coils are needed.

MOT Coils

Using specialized copper tube for the MOT coils was determined to be prohibitively expensive. Tube easily obtainable[h] from any hardware store was used along with basic epoxy and Kapton insulating tape, wrapped very carefully around the tube. A brass form was created around which the coils were wound, using a massive and time-proven lathe. The initial designs (before custom power supplies were ordered) were alternating layers of four and five windings, four layers thick. The final version was five and six windings, six layers thick. The water cooling allowed extremely high current, roughly 450A, to flow without difficulty. This configuration produced gradients of roughly $0.8\frac{G}{cm \cdot A}$.

TOP Coils

The TOP coils required significantly more effort to construct. Given the high response characteristics required by magnetic fields varying on the kHz scale and smooth predictable potential surfaces in the trap, any metal in the coil holding construct was completely out of the question. The coil forms were cut by the author out of fiberglass-epoxy composite material. Small copper wire was wound into a special heavy-duty epoxy chosen specifically for this purpose.

Two generations of forms were created, both wound. The first generation was very basic and only one pair of coils was built. These eventually failed due to metal fatigue of the wire after being used for several tests on the basic

[h] Refrigerator tube, 1/4" OD

concept. The second generation (shown in Fig. 4.6)were designed around the pairs of coils being directly interlocked and glued together, then mounted to an external gantry of the same material.

Tolerances on the forms were kept as tight as possible. The material and the dust created by cutting is highly abrasive; each cut would reduce the size of the cutter on a measurable level. Measurements were required every few cuts to maintain compliance.

Chapter 5

Cold Rubidium Clouds: MOT Performance

The performance of a MOT is determined by the time to load the MOT, the number of atoms available for experiment, their temperature and the reproducibility of these numbers. In this chapter a brief summary of the quantitative results obtained during the author's time in the lab are presented. Data acquisition techniques are discussed and some images are included.

Many parameters affect these numbers; optimization is nontrivial. Short loading times indicate high background pressures, while high background pressures can reduce atom number if the cloud is not transported out of the high pressure region fast enough. Extremely rapid movement can fatigue the transport system or even heat the cloud. During the author's time in the lab, optimization of trapped atom number was performed, but more in a spirit of diagnostics (e.g. can it perform) than an attempt to push or even establish the limits of the system. Diode failures in the midst of data sets, rearrange-

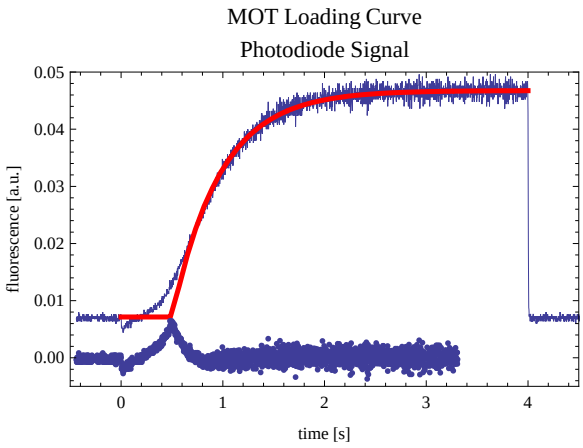

Figure 5.1: Loading curve as recorded by photodiode in a simple fluorescence configuration. Intensity units are arbitrary; data is clearly offset by ambient light. The ^{87}Rb background pressure was at $3 * 10^{-9}$ Torr. An exponential fit was performed on data from 0.5s onwards. 'Error' (data minus fit) is plotted on the same graph. It was concluded that the power supply in use at the time could not regulate quickly at low currents. A new power supply eventually replaced it, after the author's time in the lab. Loading constants were extracted from this data; the e^{-1} time was 0.47 s.

ment/restructuring of the cooling sequence and commissioning of the second lowest-pressure portion of the system necessitated further optimization, not covered here.

5.1 Imaging Techniques

Simple loading curves (Fig. 5.1) were obtained by placing a photodiode near the cold cloud. A short telescope using a pinhole spatial filter was set up between the diode and the MOT in order to increase signal-to-noise ratio. As this curve was intended only for purposes of extracting the loading time, the distances and solid-angles involved are unnecessary.

Beyond this simple diagnostic photodiode measurement, two primary meth-

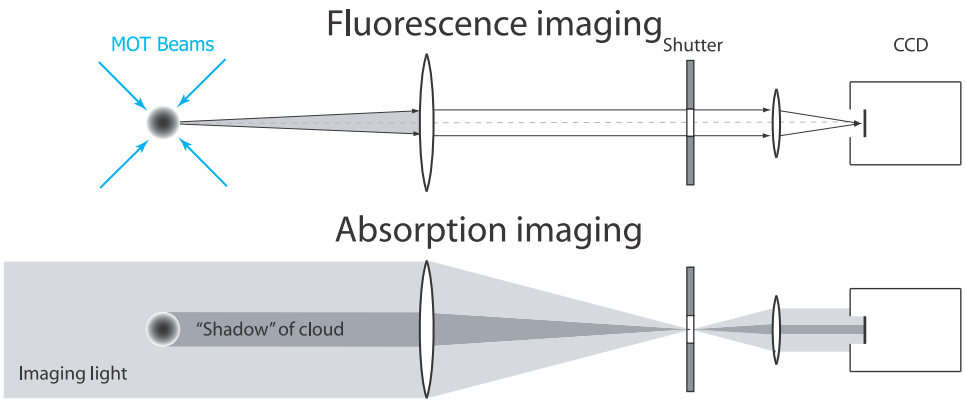

Figure 5.2: Two methods of imaging used. The telescopes involved were well characterized, giving relevant solid angles.

ods of imaging are used: absorption and fluorescence (See Fig. 5.2). In both cases, a high-speed large-well-depth PIXIS camera manufactured by Princeton instruments was used. The quantum efficiency of this camera was measured by B. Dixon[28].

To measure the quantum efficiency of the camera, the conversion from photons to counts was required. A known intensity of light was sent into the camera; this was measured with a power meter and then reduced in a known way (to avoid camera saturation) via neutral density filters. Several camera configurations were explored during the construction and testing of the first half of the system.

To manage the recording of images, the author wrote several simple visual basic scripts. One example would prompt for a region of interest, then continuously take images every time the camera received a TTL trigger. All of the scripts would process the image (and only the region of interest) as follows. Three separate images were recorded: with atoms ('data'), without atoms ('background') and without light ('dark'). Rather than import all of

these into our analysis pipeline and then perform normalization, this was taken care of within the imaging program, post-crop.[a]

5.1.1 Absorption

For absorption imaging, a collimated beam of light is projected onto the cloud, then reduced and projected onto the camera. The data is then a two-dimensional map of number-of-atoms in a column. To extract the information, we process the data image as follows.

$$I_{\text{result}} = \frac{I_{\text{data}} - I_{\text{dark}}}{I_{\text{bg}} - I_{\text{dark}}}$$

This is done on a pixel-by-pixel basis, normalizing the result image to relative intensity values. The absolute beam intensity is unnecessary information (as long as the atoms are not saturated by the imaging light), as we will see.

The absorption of light by dilute media (each column of atoms along the z-direction) was first discussed by Rayleigh long ago; particles in the media are assigned a scattering cross section σ_{cs} and each collision results in loss of light, as the directionality of the light is very likely changed:

$$\begin{aligned} dI(\vec{x}) &= -\alpha(\vec{x})I(\vec{x})dz \\ \alpha(\vec{x}) &= \sigma_{cs}N(\vec{x}) \end{aligned} \tag{5.1}$$

where I is the intensity of light, $N(\vec{x})$ is the number density of atoms and α is the media-dependant absorption coefficient. The scattering cross section can

[a]This image pipeline saved many hours of time during calibration of the system parameters.

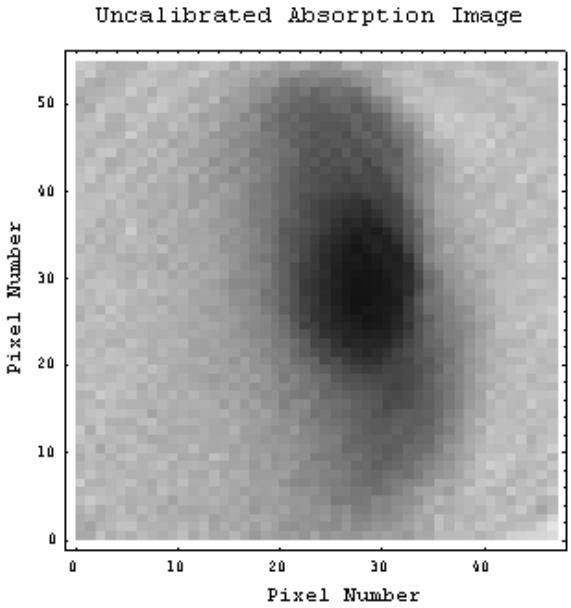

(a) Absorption image of MOT. Summation of columns shown below. Note ripple-like distortions due to multiple pieces of glass between source and camera.

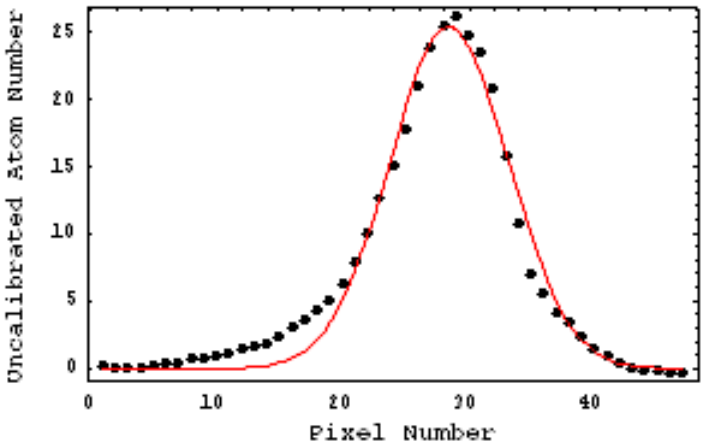

(b) Plot of uncalibrated atom number. Columns above summed into a single row.

Figure 5.3: Uncalibrated absorption image taken in Sept. 2006. Images taken during this period were an attempt to get consistent, predictable data from MOT to MOT. In order to calibrate this image, a great deal more information regarding the instantaneous detuning of the laser as well as the geometry of the temporary setup employed would be required. This imaging method was neglected during the author's time in the lab due to various technical difficulties.

be derived straightaway from the scattering rate:

$$\gamma_p = \frac{s_0\gamma/2}{1 + s_0 + (2\delta/\gamma)^2} \qquad [3.2]$$

The cross section (for one atom) combined with intensity will give the scattered energy; the scattering rate (for one atom) and the energy of the scattered light will also give the scattered energy, linking the two.

$$\sigma_{cs} I = \hbar\omega\gamma_p$$

Note that the scattering rate depends on the ratio of intensity to saturation intensity. Imaging light will be as weak as is reasonable, avoiding saturation by a wide margin. Let us derive the atom density from the two-dimensional intensity map recovered by the CCD. With $N(\vec{x}) = \frac{dN}{dAdz}$, we have

$$dI(\vec{x}) = -\sigma_{cs}\frac{dN}{dA\cancel{dz}} I(\vec{x})\cancel{dz}$$

We will be using pixels of the camera as the units of area in this measurement. Naturally, via telescopes shown in Fig. 5.2, the image will be expanded to fill a sufficient fraction of the CCD that variation across the pixels will be minimal.

$$\begin{aligned} dN &= \frac{-A}{\sigma_{cs}} \frac{dI(\vec{x})}{I(\vec{x})} \\ N(x,y) &= \frac{-A}{\sigma_{cs}} ln(\frac{I}{I_0}) \end{aligned} \qquad (5.2)$$

As the telescopes and the specifications of the camera are theoretically known, so A is theoretically known. The earlier mentioned image normalization leads to direct knowledge of I and I_0. We now know the number of atoms in each

pixel-column. In practice, during our first-attempt setups, fine control over a beam traversing the entire machine was somewhat more difficult than expected.

The image is a projection of the 3-d density cloud into a two-dimensional image. Integrating over the cloud density yields the total number of atoms.

One problem with this method is fast control of light. The absorption method requires trapping beams to be inactive, thus the imaging light must be turned on rather quickly. The duration of the imaging pulse must not saturate the camera or allow the atoms to significantly fall during image capture. Much light-switching is accomplished via the AOMs[b], but there are several shutters in the system. As the scattering rate is dependant on the detuning of the light, the mechanical shock from these shutters was a significant effect in disrupting the 'instantaneous' lock of the laser frequency; that is, the detuning of the laser during image capture. This problem was somewhat solved by 'soft-mounting' the shutters on absorptive material.[c] While many of these bugs were being worked out in the first months of imaging, we relied on fluorescence for our data.

5.1.2 Fluorescence

Fluorescence imaging works by collecting the scattered light from atoms and focusing an image on the camera. The image processing is slightly different;

$$I_{result} = I_{\text{data}} - I_{\text{bg}}$$

[b] see Sec. 4.1.1

[c] A variety of sorbothane pieces were used.

This washes out dark current without requiring a specific image for that purpose. We found fluorescence imaging to be more robust, in contrast to absorption.

To calculate[d] the atom density from this resultant image (pixels containing $c(x, y)$ counts), we must know the appropriate solid angle (Ω), losses due to optics (0.96^r w/ r = number of non-AR surfaces), the scattering rate (Eq. 3.2), exposure time (t_{exp}), the quantum efficiency of the camera (q) and the conversion from photon energy to number of electrons excited p.

$$N(x, y) = \frac{4\pi}{\Omega} \frac{c(x, y)q}{p\gamma_p 0.96^r}.$$

As the cloud is very small compared to the Rayleigh range of the telescope system, the entire cloud should be sufficiently in focus and the image is a map of column counts. The total atom number can be calculated easily by summing all the pixels.

One problem with this method is reflections from the apparatus itself; light scattered away from the camera and thus not expected by this calculation may be reflected by components back into the imaging system, registering false counts. For the most part, this was limited to small areas that could be ignored by analysis software.

[d] This discussion follows [28].

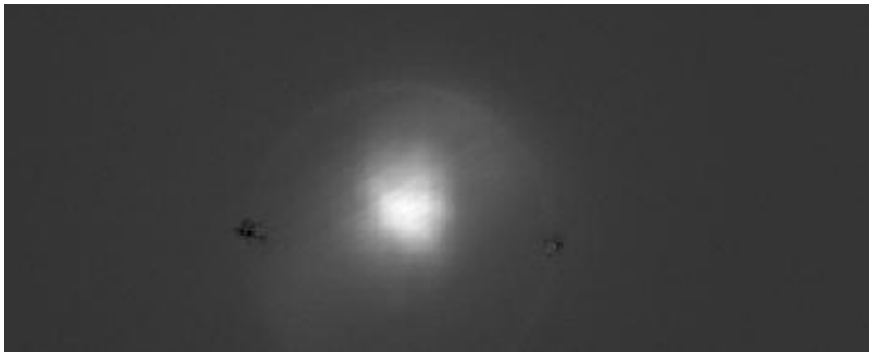

(a) Fluorescence image of MOT. Summation of columns shown below. Note blocked out reflections.

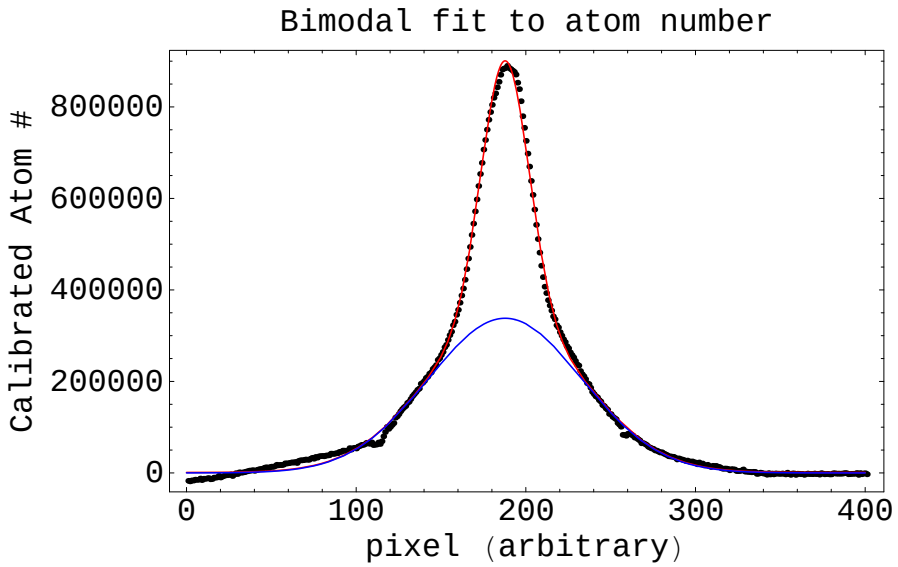

(b) Plot of atom number. Columns above summed into a single row.

Figure 5.4: This data is from the first set of MOT coils in an early imaging configuration, April 2006. Most of the population is in the outer region. Atom numbers for this data were estimated at 3×10^9 in the central feature, with 11×10^9 total atoms. Typical parameters were better tuned, placing nearly all atoms in the central feature. This particular MOT image was chosen to exemplify the two-component regime. Sub-Doppler cooling is based on the shifts of sublevels due to the surrounding light. When the shifts from magnetic fields in a MOT are comparable to the light shifts, sub-Doppler cooling occurs is no longer effective. Thus a MOT can have two cooling regions, a sub-Doppler volume and an outer region which is less-dense with higher temperature.[7]

5.2 Temperatures: TOF

The two invaluable numbers that can be extracted from these pictures are atom number and temperature. To obtain the former, all that is required is simple calibrated addition of pixel values in one image; the latter requires a sequence of images in time. Free expansion of a trapped cloud was used to determine the temperature: by finding the rate of expansion of the cloud, we can discern the average velocity and thus the temperature of the cloud. This is one version of time-of-flight (TOF) temperature determination.

It is a reasonable assumption that the three dimensional density distribution of trapped atoms is very close to a gaussian in form,

$$n(\vec{s}, t = 0) = \frac{n_t}{(\sqrt{2\pi}\sigma_s)^3} e^{-\frac{\vec{s}\cdot\vec{s}}{2\sigma_s^2}}.$$

Here n_t is the total number of atoms and σ_s is the width of the distribution in a given dimension. This can, of course, be decomposed into three separate gaussian distributions which can be integrated separately. This would allow for different sizes in different dimensions, as is the case with our MOT: the field is twice as strong in the vertical dimension. This is no matter, however, as each dimension is independent of the other.

It is straightforward to find the distribution of atoms after a given time t. Using a Dirac-delta function and the relevant Maxwell-Boltzmann distribution,

we can find the atoms able to make it to any given location:

$$n(\vec{s},t) = \int_{-\infty}^{\infty} d\vec{v} \int_{-\infty}^{\infty} d\vec{s_i}\ n(\vec{s_i}) f(\vec{v}) \delta(\vec{s_i} - \vec{s} + \vec{v}t)$$

$$n(\vec{s},t) = \frac{N}{(\sqrt{2\pi}\sigma_{s_i})^3} \sqrt{\left(\frac{m}{2\pi kT}\right)^3} \int_{-\infty}^{\infty} d\vec{v} \int_{-\infty}^{\infty} d\vec{s_i}\ e^{-\frac{\vec{s_i}\cdot\vec{s_i}}{2{\sigma_{s_i}}^2}} e^{-\frac{m\vec{v}\cdot\vec{v}}{2kT}} \delta(\vec{s_i} - \vec{s} + \vec{v}t)$$

where $\vec{s_i}$ is some dimension. If one wishes to find the full expression, each dimension will have its own integral. It is possible to use only one dimension, as done with the analysis used for Fig. 5.5b. Here $f(\vec{v})$ is an amalgam of three one-dimensional Maxwell-Boltzmann distributions, all given the same temperature. After a fair bit of algebra, one recovers

$$n(\vec{s},t) = \frac{N}{\sqrt{2\pi}^3 {\sigma_s(t)}^3}\ e^{-\frac{{s_x}^2}{2\sigma_s(t)}} \tag{5.3}$$

$$\sigma_s(t) = \sqrt{\tfrac{kT}{m}t^2 + {\sigma_{s_i}}^2} \tag{5.4}$$

This is another Gaussian, but with variable width $\sigma_s(t)$ which will allow us to measure the temperature via a well-timed sequence of images of the MOT's expansion.

The obvious problem to this method is the reproducibility of a cold cloud at given experimental parameters; the available imaging methods are destructive to such a free-expansion MOT. With care it is possible to consistently produce similar clouds. As such, sequences were taken with varied delay between MOT release and image capture.

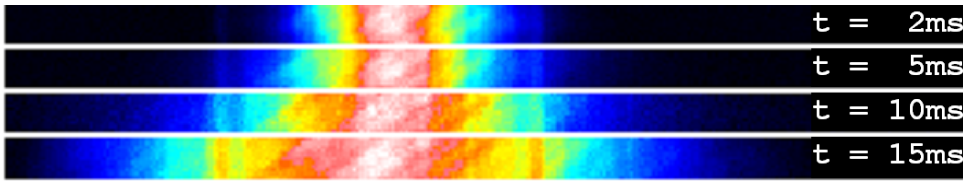

(a) Sequence of multiple fluorescence images of MOT. Different times from different MOTs. Sigma was found for each frame.

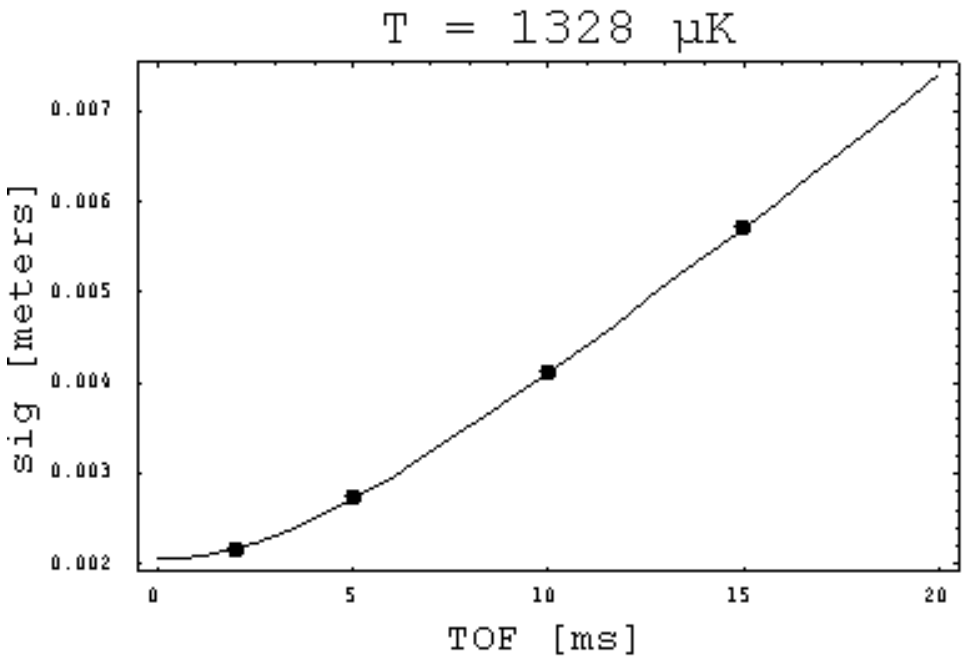

(b) Plot of sigma versus time. Fit resulted in an estimated temperature of $1.3\mu K$.

Figure 5.5: Time-of-flight image taken in October, 2006. The images in 5.5a represent a thin slice through the center of the cloud. At t=15ms, light reflected from the differential pumping tube behind the cloud is clearly visible. This ring-shaped region was excluded from the fit. This fit estimated the atom number at $3.4 * 10^7$. Many runs were made with a variety of detuning values (for the cycling light) and for repump power values. Trends were established, allowing for rudimentary optimization. This is one of the earliest optimizations based on these parameters and was repeated later.

5.3 Conclusions

Working with Prof. Schneble and fellow students H. Ruf, R. Schiller and S. Albert, the first complete MOT system was characterized. Traps capable of holding $\sim 10^8$ atoms were observed in early configurations, with temperatures in the micro-kelvin range without a great deal of fine-tuning required. Many improvements from these first estimates were made during the author's time in the lab, and surely have been made since.

Some advantages and strong points of the system were fortuitous. The physically separate tables for lasers and the trapping apparatus lent the laser lock easy sustainability to within fractions of the natural linewidth, even during use of the mechanical translator. Some were hard fought, such as the exact configuration of the MOT coils and coil holder, currently on versions four and two respectively. The imaging system is flexible and has served in multiple configurations, seamlessly integrated with data collection. Some struggles have been ongoing, most significantly the quality of the laser diodes supplied by the vendors.

With a MOT ready and in the secondary cooling system in roughly one minute, the system performs quite well. By the conclusion of the author's time in the lab, the BEC portion of the system was pumped down below measurable levels and tests were being performed on the quality of transport scheme and the trap lifetimes possible there.

Bibliography

[1] Helge Kragh. Max Planck: The Reluctant Revolutionary. Physics World, December 2000.

[2] Summary of proceedings of Mini-symposium: The Birth of Quantum Theory, December 2000. URL http://physics.ucsc.edu/~michael/planck.html.

[3] C. Davisson and LH Germer. The scattering of electrons by a single crystal of nickel. Nature, 119:558–560, 1927.

[4] O. Theimer and Budh Ram. The beginning of quantum statistcs. American Journal of Physics, 44(11), November 1976.

[5] M. Delbruck. Was Bose-Einstein statistics arrived at by serendipity? Journal of Chemical Education, 57:467–470, 1980.

[6] A. Einstein. Quantentheorie des einatomigen idealen Gases. Akad. d. Wiss. Berling, Sitzungsber Phys. Math. Kl., 22, 1924.

[7] C. G. Townsend, N. H. Edwards, C. J. Cooper, K. P. Zetie, C. J. Foot, A. M. Steane, P. Szriftgiser, H. Perrin, and J. Dalibard. Phase-space density in the magneto-optical trap. Phys. Rev. A, 52(2):1423–1440, Aug 1995.

[8] H. Lewandowski, D. Harber, D. Whitaker, and E. Cornell. Simplified System for Creating a Bose–Einstein Condensate. Journal of Low Temperature Physics, 132(5):309–367, 2003.

[9] Harold J. Metcalf and Peter van der Straten. Laser Cooling and Trapping. Springer-Verlag, 1999.

[10] D. J. Wineland and Wayne M. Itano. Laser cooling of atoms. Phys. Rev. A, 20(4):1521–1540, Oct 1979.

[11] S. Chu, J. E. Bjorkholm, A. Ashkin, and A. Cable. Experimental observation of optically trapped atoms. Phys. Rev. Lett., 57(3):314–317, Jul 1986.

[12] Utaka Yoshikawa, Takeshi Umeki, Takuro Mukae, Yoshio Torii, and Takahiro Kuga. Frequency stabilization of a laser diode with use of light-induced birefringence in an atomic vapor. Applied Optics, 42(33):6645–9, 2003.

[13] Joseph H. Eberly and Peter W. Milonni. Lasers. John Wiley & Sons, 1988.

[14] Wolfgang Demtröder. Laser Spectroscopy. Springer-Verlag, 3rd edition, 2003.

[15] R.P. Feynman, F.L. Vernon Jr, and R.W. Hellwarth. Geometrical Representation of the Schrödinger Equation for Solving Maser Problems. Journal of Applied Physics, 28:49, 1957.

[16] Daniel A. Steck. Rubidium 87 D Line Data. URL http://steck.us/alkalidata/. oct 2003.

[17] Irina Novikova, Andrey B. Matsko, and George R. Welch. Influence of a buffer gas on nonlinear magneto-optical polarization rotation. J. Opt. Soc. Am. B, 22(1):44–56, 2005.

[18] S. Brandt, A. Nagel, R. Wynands, and D. Meschede. Buffer-gas-induced linewidth reduction of coherent dark resonances to below 50Hz. Phys. Rev. A, 56(2):R1063–R1066, Aug 1997.

[19] C P Pearman, C S Adams, S G Cox, P F Griffin, D A Smith, and I G Hughes. Polarization spectroscopy of a closed atomic transition: applications to laser frequency locking. Journal of Physics B: Atomic, Molecular and Optical Physics, 35(24):5141–5151, 2002. URL http://stacks.iop.org/0953-4075/35/5141.

[20] L. Ricci, M. Weidemüller, T. Esslinger, A. Emmerich, C. Zimmermann, V. Vuletic, W. König, and T. Hänsch. A compact grating-stabilized diode laser system for atomic physics. Optics Communications, 117:541–9, 1995.

[21] Paul D. Lett, Richard N. Watts, Christoph I. Westbrook, William D. Phillips, Phillip L. Gould, and Harold J. Metcalf. Observation of atoms laser cooled below the doppler limit. Phys. Rev. Lett., 61(2):169–172, Jul 1988.

[22] Luis A. Orozco. Laser cooling and trapping of neutral atoms. In S. Hacyan, R. Jauregui, and R. L. Pea, editors, The XXXI Latin-American School of Physics New Perspectives on Quantum Mechanics, pages 67–90. AIP Conference Proceedings 464, 1999.

[23] A. M. Steane, M. Chowdhury, and C. J. Foot. Radiation force in the magneto-optical trap. J. Opt. Soc. Am. B, 9(12):2142–58, dec 1992.

[24] C. Monroe, W. Swann, H. Robinson, and C. Wieman. Very cold trapped atoms in a vapor cell. Phys. Rev. Lett., 65(13):1571–1574, Sep 1990.

[25] Arjen Amelink. Photoassociation of Ultracold Sodium Atoms. PhD thesis, Utrecht University, feb 2000.

[26] VacIon Plus 150 pumps. Varian Inc., April 2006.

[27] Alan L. Migdall, John V. Prodan, William D. Phillips, Thomas H. Bergeman, and Harold J. Metcalf. First observation of magnetically trapped neutral atoms. Phys. Rev. Lett., 54(24):2596–2599, Jun 1985.

[28] B. Dixon. MOT Characterization with a CCD Camera. Optics Rotation Presentation at SUNY Stony Brook, March 2006.